the plant journal

SEB SOCIETY FOR EXPERIMENTAL BIOLOGY

The Plant Journal (2025) **122,** e70227 doi: 10.1111/tpj.70227

TECHNICAL ADVANCE

Synchrotron macro-ATR-FTIR: a powerful technique for analyzing changes in plant cell chemical composition after surfactant exposure

Thi Linh Chi Tran[1], Annaleise R. Klein[2], Jitraporn Vongsvivut[2], Yichao Wang[3], Lingxue Kong[4], Wenrong Yang[1] and David Cahill[1,*]

[1]*School of Life and Environmental Sciences, Deakin University, Waurn Ponds Campus, Geelong, Victoria 3216, Australia,*
[2]*Australian Synchrotron, Australian Nuclear Science & Technology Organisation, 800 Blackburn Road, Clayton, Victoria 3168, Australia,*
[3]*School of Science, RMIT University, Melbourne, Victoria 3000, Australia, and*
[4]*Institute for Frontier Materials, Deakin University, Waurn Ponds Campus, Geelong, Victoria 3216, Australia*

Received 25 February 2025; revised 2 May 2025; accepted 7 May 2025.
*For correspondence (e-mail david.cahill@deakin.edu.au).

SUMMARY

Surfactants, as foliar sprays, are widely used to increase the uptake of agrichemicals through plant leaf surfaces. Study of the effects of surfactants on plants has mainly focused on investigation of the mechanisms that underlie changes in droplet behavior on leaf surfaces. However, how surfactants may affect leaf chemical composition is largely unknown. The standard analysis techniques that have been widely used for leaf chemical analyses such as mass spectroscopy require complex and extensive sample preparation and leaf tissue destruction. Here, we have used an advanced technique, synchrotron macro-Attenuated Total Reflectance-Fourier Transformed InfraRed spectroscopy (synchrotron macro-ATR-FTIR), which provides a fast, non-destructive and *in vivo* method to capture the leaf surface and enable the chemical mapping of essential functional groups. The development of two Quasar workflows for analyzing complex FTIR data in this study highlights and strengthens the advantages of synchrotron macro-ATR-FTIR for plant research. We found that the treatment of 5-week-old maize (*Zea mays* L.) leaves with a commercial surfactant, Silwet-L-77, resulted in alterations in the FTIR spectral signatures associated with lipids, proteins and carbohydrates commencing 1 h after treatment. The effects of the surfactant on maize leaf water droplet behavior and photosynthetic performance were concentration-dependent. Synchrotron macro-ATR-FTIR is thus a newly emerging and powerful analytical technique for quantitative studies in plant physiology and biochemistry, especially for plant responses to external environmental factors including both abiotic and biotic stresses.

Keywords: epicuticular wax, epidermis, maize, leaf surface, synchrotron, ATR-FTIR, surfactant, Quasar, hyperspectra.

INTRODUCTION

In recent years, vibrational spectroscopy techniques, particularly Fourier Transform Infrared (FTIR) spectroscopy, have gained increasing attention in plant research (Cuello et al., 2020; Khambatta et al., 2021; Willick et al., 2018). The distinct advantages of this technique are the ability to allow direct and *in situ* measurements together with spatially resolved chemical information for plant samples (Vongsvivut et al., 2019). Based on the principle that molecular bonds absorb infrared radiation at specific wavelengths corresponding to their vibrational modes, FTIR provides detailed molecular chemical structures and the composition of biological samples based on these specific vibration spectra (Morais et al., 2020). In combination with microscopy, FTIR microspectroscopy enables the spatial mapping of chemical functional groups at intermediate resolutions, ranging from 0.5 to 25 μm, and according to Khambatta et al. (2021) depends on factors such as the type of instrument, optical components and light source. When coupled with the attenuated total reflectance (ATR)

mode, Baker et al. (2014) demonstrated that FTIR was also able to analyze the surface of a sample regardless of its thickness.

One of the most significant drawbacks of benchtop FTIR systems is their lower spatial resolution, primarily due to the limited brightness of standard thermal infrared light sources. This limitation restricts its ability to perform high-resolution measurements at the single-cell level, which is crucial in many biological applications (Miller & Dumas, 2006). Vongsvivut et al. (2019) overcame those limitations by using synchrotron ATR-FTIR with a broad-band high-brightness synchrotron IR beam which offered 100–1000 times higher brightness than a conventional thermal light source in a laboratory-based FTIR microspectroscopic instrument. This advantage allowed a significantly higher signal-to-noise ratio, enabling molecular characterization of individual cells. Synchrotron macro-ATR-FTIR uses a large ATR hemispherical element and a single-point detector in mapping mode, leading to an increased field of view and only requiring a single contact point for the entire mapping measurement.

With the advantages of a synchrotron light source, synchrotron ATR-FTIR enables shortened data acquisition times. For example, in the study presented here, a high-resolution chemical map of leaves over an area of 100 $\times$ 100 μm in size provided approximately 1500 spectra within a few hours. The data volume increases markedly when a large number of samples and replicates are required to achieve statistical robustness and reproducibility. Data handling and processing using methods such as programming scripts or using commercial software require specialized skills or lead to inflexibility due to cost and limited accessibility. In contrast, Quasar software, which was first reported by Toplak et al. (2017), is a visual and flexible add-on to the Orange Data Mining open-source toolkit that was developed for data visualization, machine learning and data mining. While Orange provides a user-friendly framework for designing customizable data processing workflows to solve machine learning problems, as described by Demsar et al. (2013), Toplak et al. (2021) demonstrated that Quasar extends Orange's capabilities to handle hyperspectral datasets and includes functionalities that are specialized for spectral data analysis. In this manuscript, we develop protocols for analyzing large volume hyperspectral data collected from plant samples using synchrotron macro-ATR-FTIR. We also highlight interactive features of the software, showcasing its advantages over other software in bio-spectroscopy data analysis for plant research.

In our study, we demonstrate the combination of synchrotron-macro-ATR-FTIR and Quasar to understand the impact of a commonly used surfactant on the chemistry of the leaf surface and near-surface cell layers. Foliar spray of agrichemicals without added surfactant provides limited uptake of the active ingredient due to the hydrophobic nature of the plant cuticle, which is primarily composed of lipid-rich compounds such as cutin and waxes (Fernandez et al., 2017; Fernandez et al., 2021). To address this impediment, surfactants are frequently employed as adjuvants to enhance the uptake and efficacy of active ingredients in various agrichemical formulations, including pesticides (Chen et al., 2024), herbicides (Appah et al., 2020), fungicides (Hu et al., 2022) and fertilizers (Magor et al., 2023).

The chemical properties of surfactants play an important role in their interactions with the plant leaf surface. Amphiphilic surfactants are categorized into two major groups based on their head group characteristics, each paired with a hydrophobic tail (Baales et al., 2021): (1) non-ionic surfactants with an uncharged head group and (2) ionic surfactants, which include anionic surfactants with a negatively charged head group and cationic surfactants with a positively charged head group. Non-ionic surfactants have been reported by Castro et al. (2013) and more recently by Congreve and Cameron (2019) to be the most commonly used additives in either spray formulation or spray tank mixes. The mechanisms by which surfactants facilitate the uptake of active ingredients through the hydrophobic barrier of the plant cuticle have been well documented. It involves (1) increasing the retention, spreading and coverage of the droplets on leaf surfaces (Zheng et al., 2021), (2) enhancing leaf surface wettability by decreasing the contact angle between droplets and the plant surface (Zhou et al., 2018) and (3) inducing a plasticizing effect on the transport-limiting barrier of plant cuticles (Baales et al., 2021).

Synchrotron FTIR has been used in a very limited number of plant studies to date. Kerr et al. (2013), for example, used this method to determine the mechanism of leaf lignin decomposition. Thumanu et al. (2017) applied this method to investigate the resistance against anthracnose disease in chili (*Capsicum annuum* L.) while Willick et al. (2018) used it to examine the response to cold stress of wheat (*Triticum aestivum* L.). To our knowledge, there has been only one previous study using synchrotron ATR-FTIR (Khambatta et al., 2021) where live and intact plant leaf tissues were analyzed. Here, we demonstrated that the application of a surfactant causes alteration in the biochemical composition of plant leaves. We also show that synchrotron macro-ATR-FTIR reveals changes in major macromolecules of the plant leaf surface and provides unprecedented high spatial resolution information.

RESULTS

Silwet-L-77 increases the wettability of the plant leaf

The contact angles of water droplets or Silwet-L-77 solutions (0.02%, 0.2% and 2%) were measured on five-week-old maize leaves (Figure 1). The water contact angle of the control group remained constant at approximately 136.0°

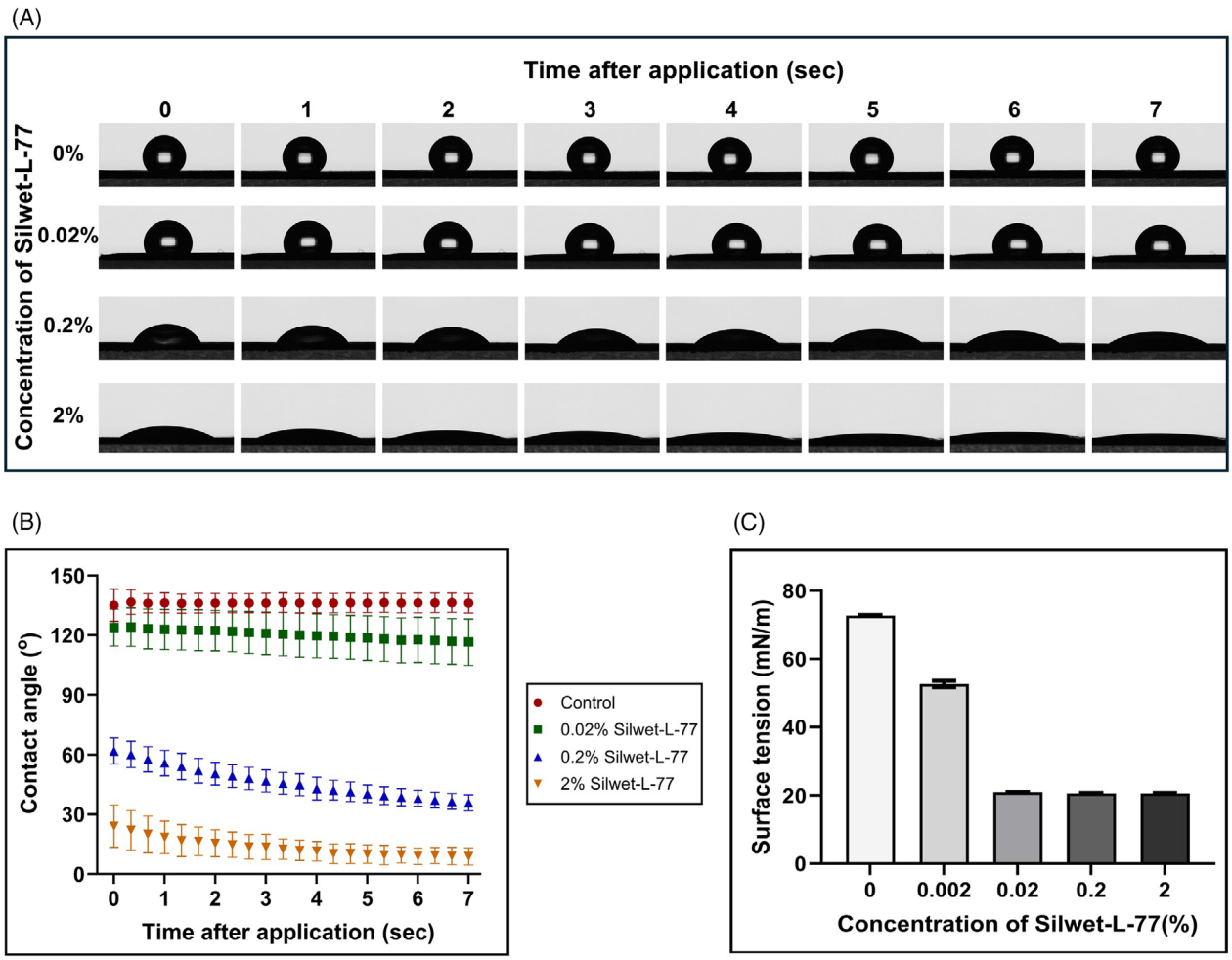

Figure 1. The effects of different concentrations of Silwet-L-77 on droplet behaviors on a maize leaf.
(A) Representative optical images of droplets of DI water or Silwet-L-77 solutions on maize leaf surface at different time points after application.
Contact angle (B) and surface tension (C) of Silwet-L-77 solutions at different concentrations. Error bars represent two standard deviations of the mean.

across all time points and indicated the hydrophobic nature of the plant leaf. The 0.02% Silwet-L-77 reduced the contact angle to 116.5° within 7 sec of the application. As the Silwet-L-77 concentrations increased to 0.2% and 2%, the contact angle exhibited a faster reduction over time, to approximately 35.8° and 8.9° at 7 sec, respectively (Figure 1A,B). This indicates a significant increase in the wettability of the maize leaf surface induced by the surfactant treatments. The surface tension of water greatly reduced from 72.8 to 52.6 mN/m by the addition of a small amount of 0.002% Silwet-L-77, which was further reduced to 21.0 mN/m when 0.02%–2% of Silwet-L-77 were added (Figure 1C).

Changes in maize leaf surface morphology induced by surfactant application

The morphology of the maize leaf surface in the control and Silwet-L-77-treated samples was observed using SEM (Figure 2). On an adult maize leaf, the cuticle is covered by a dense layer of epicuticular wax crystals, which are typically nanoscale and characterized as 'plates or platelets' arranged in an unstructured manner (Barthlott et al., 1998; Nadiminti et al., 2015). The solubility of wax platelets was increased after spraying with increasing surfactant concentrations. This effect was more pronounced when the samples were washed with water post-treatment, as the crystalloids were dissolved by the surfactant and subsequently removed by the washing step. In addition, the leaf epicuticular wax structures showed an amorphous appearance instead of the typical platelet-like structure.

Photosynthetic performance of leaves is reduced following treatment with high concentrations of surfactant

The ability of Silwet-L-77 to enhance wettability on maize was demonstrated through contact angle measurements, surface tension analysis and SEM imaging

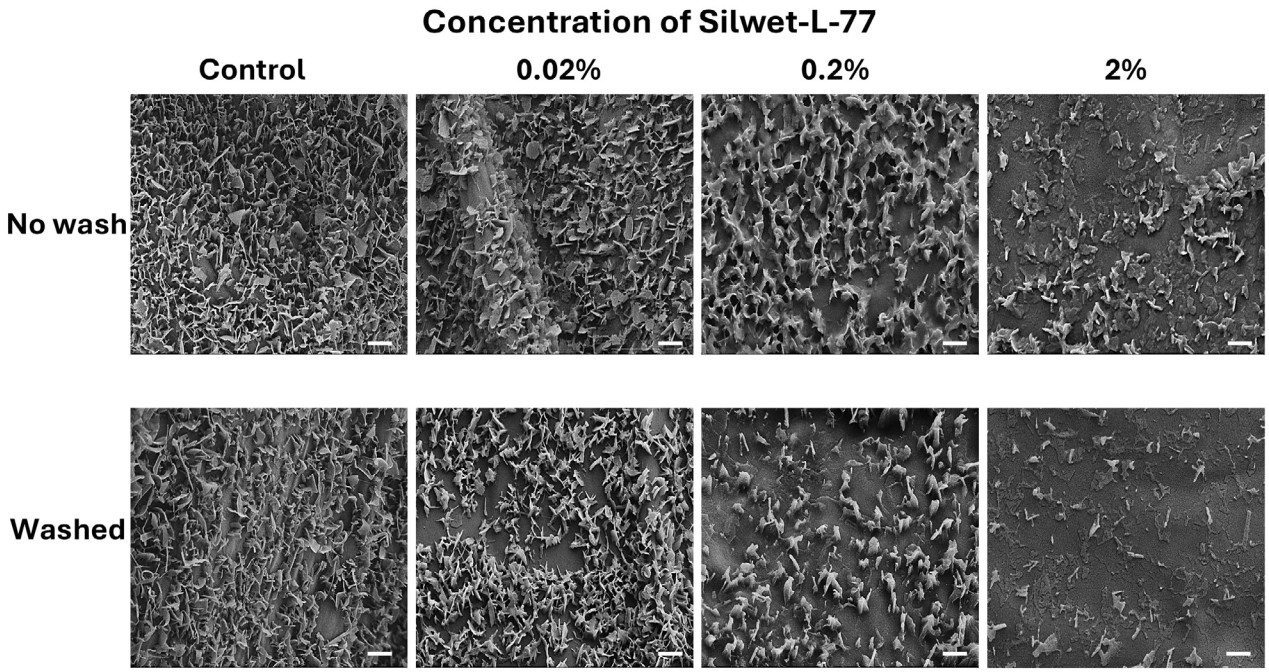

Figure 2. Representative SEM images of the adaxial leaf surface of maize after 1 h of treatment with Silwet-L-77.
Following treatment with the surfactant, the leaf samples were either left without further washing (upper row of images) or subjected to a single wash with deionized water (lower row of images). Treatment with the surfactant disrupted wax platelets on the maize leaf surface in a concentration-dependent manner and washing with water removed wax debris. Scale bar: 1 μm.

(Figures 1 and 2). To determine whether the concentrations of Silwet-L-77 used have adverse effects on maize leaves, we evaluated their photosynthetic performance (Figure 3). Chlorophyll fluorescence parameters were obtained for dark-adapted leaves in both control and surfactant-treated samples 1–24 h after treatment. For each sample, a rapid light curve with photosynthetically active radiation (PAR) value ranging from 0 to 403 μmol/m^2/sec was initiated. Representative images of the maximum quantum efficiency of PSII (Fv/Fm, measured at PAR = 0) for maize leaves treated with different concentrations of Silwet-L-77 were shown in Figure 3A. When compared to the control, no color change was observed for 0.02% Silwet-L-77, whereas 0.2% and 2% treatments showed a shift from violet and blue to light green in the middle and edges of the leaves, indicating a reduction in Fv/Fm values. Treatment with 2% Silwet-L-77 reduced the Fv/Fm ratio from 0.75 in control leaves to 0.63 after 24 h (Figure 3B). For comparisons between different time points, data for photosynthetic parameters were extracted at a PAR of 111 μmol/m^2/sec, as this level remains below the saturation point (~185 μmol/m^2/sec) observed in the rapid light curve (Figure S1). This allows the detection of subtle differences in photosynthetic responses without the influence of photoinhibitory effects (Figure 3C–I). For all parameters in Figure 3C–I, there were no significant differences observed between samples within 1 h after the surfactant treatment as well as between the control and 0.02% Silwet-treated leaf at all time points.

Treatment with Silwet-L-77 caused the PSII effective quantum yield (ΦPSII) to decrease, starting at 6 h for the 2% concentration and 12 h for the 0.2% concentration (Figure 3C). The values of ΦPSII reached their lowest at 24 h after treatment, as shown by reductions of 40.4% and 66.3% compared to control for 0.2% and 2% Silwet-L-77, respectively. The most significant differences for the

Figure 3. Chlorophyll fluorescence parameters of Silwet-L-77-treated maize leaves.
(A) Representative images of the Fv/Fm obtained by an IMAGING-PAM at PAR = 0; (B) Fv/Fm, maximum quantum efficiency of PSII; (C) ΦPSII, PSII effective quantum yield; (D) ΦNPQ, quantum yield of regulated energy dissipation; (E) ΦNO; quantum yield of non-regulated energy dissipation; (F) NPQ, non-photochemical quenching; (G) qN, coefficient of non-photochemical quenching (lake model, collective energy dissipation across interconnected PSII units); (H) qP, coefficient of photochemical quenching (puddle model, each PSII unit is independent with absorbed energy remaining localized); (I) qL, coefficient of photochemical quenching (lake model).
Bars represent standard deviation of the mean (n = 5). Different letters indicate significant differences (P < 0.05) between samples within a common timepoint as determined by two-way ANOVA followed by Tukey's HSD post hoc test. Note that chlorophyll fluorescence parameters have no units, as they are typically expressed as ratios.

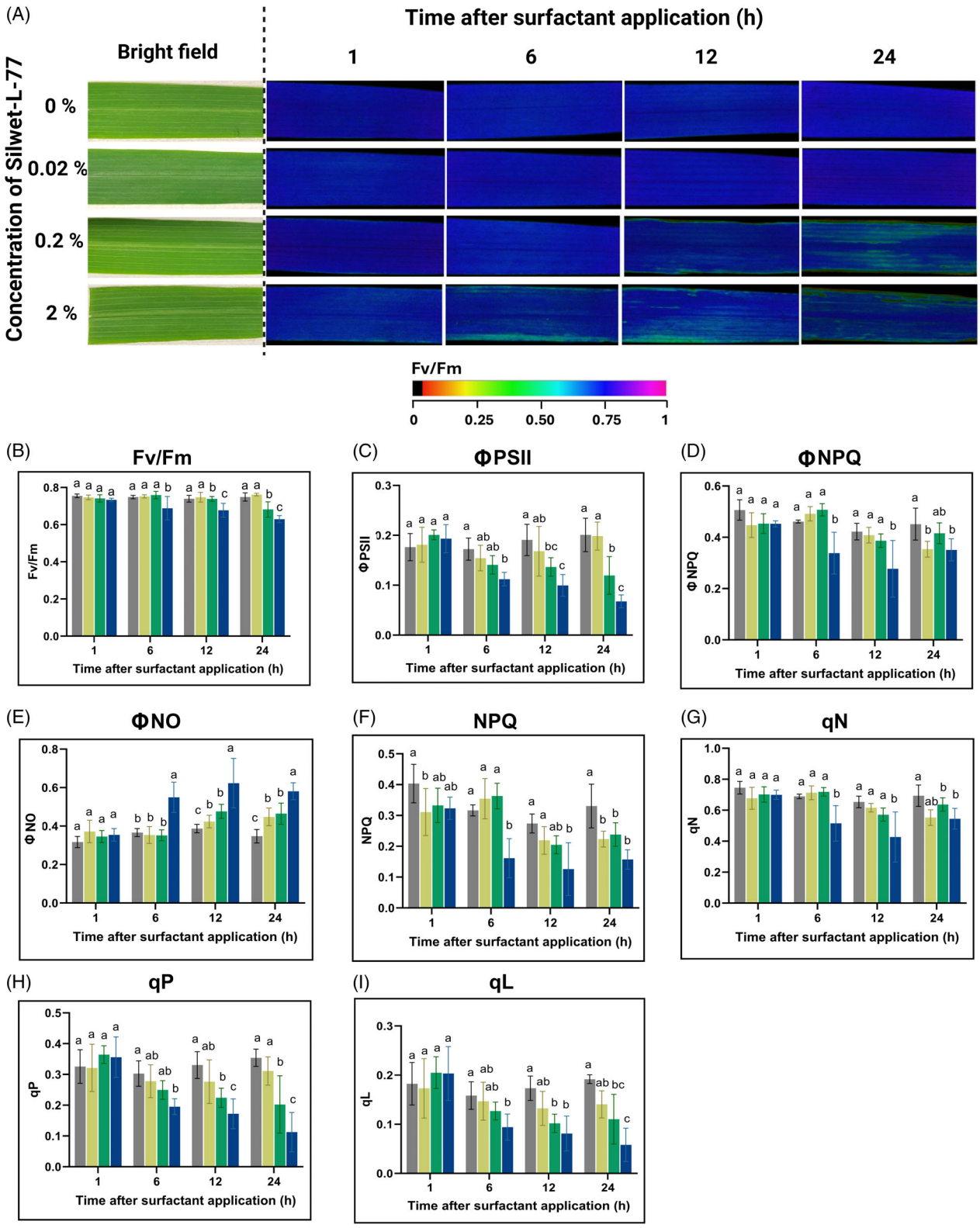

quantum yield of regulated energy dissipation ΦNPQ were observed between the 2% Silwet-L-77-treated leaves and the control leaves at 6, 12 and 24 h, with reductions in ΦNPQ of 26.7%, 46.1% and 22.2%, respectively (Figure 3D). At 12 and 24 h, greater Silwet-L-77 concentrations resulted in higher values of the quantum yield of non-regulated PSII energy dissipation ΦNO compared to control (Figure 3E). The ΦNO of the 2% Silwet-L-77-treated samples at 24 h increased by 67.2% compared to the control. For non-photochemical quenching, NPQ, at 24 h, the value for treated was significantly lower than control, with a reduction of at least 27.9% observed (Figure 3F). There was no significant difference in the coefficient of non-photochemical quenching (qN) for most treated leaves across timepoints, except for those treated with 2% Silwet-L-77 (Figure 3G). Meanwhile, a reduction of 32.1% and 47.9% in the coefficient of photochemical quenching qP (puddle model, each PSII unit is independent with absorbed energy remaining localized) was observed in leaves treated with 0.2% and 2% Silwet-L-77, respectively, at 12 h compared to the control (Figure 3H). The coefficient of photochemical quenching qL (lake model, collective energy dissipation across interconnected PSII units) showed a similar trend to qP, with greater reductions in qL observed when maize leaves were treated with higher concentrations of Silwet-L-77 (Figure 3I). While Figure 3C–I shows the effects of different Silwet-L-77 concentrations on photosynthetic parameters at PAR = 111 μmol/m^2/sec, a similar trend was observed across other light intensities throughout the entire rapid light curve. An example of the differences between treatment groups at various light intensities at 24 h is shown in Figure S1.

Synchrotron macro-ATR-FTIR identifies the changes in chemical functional groups in leaf surfaces treated with a surfactant

We discovered that high concentrations of Silwet-L-77 had negative effects on maize plants, as indicated by the photosynthetic parameters mentioned above. To gain more understanding of how these high concentrations of Silwet-L-77 affect the biochemical composition of leaves, we utilized synchrotron macro-ATR-FTIR analysis. We developed two different workflows to analyze 13 601 FTIR hyperspectra obtained in this study using the freely accessed and python-based Quasar software.

The baseline-corrected and vector-normalized average absorbance spectra collected from control maize leaves and those treated with 2% Silwet-L-77 at 1, 6 and 12 h after treatment are shown in Figure 4A. The spectra consist of the 3000–2800 cm^{-1} and 1800–970 cm^{-1} regions. There are

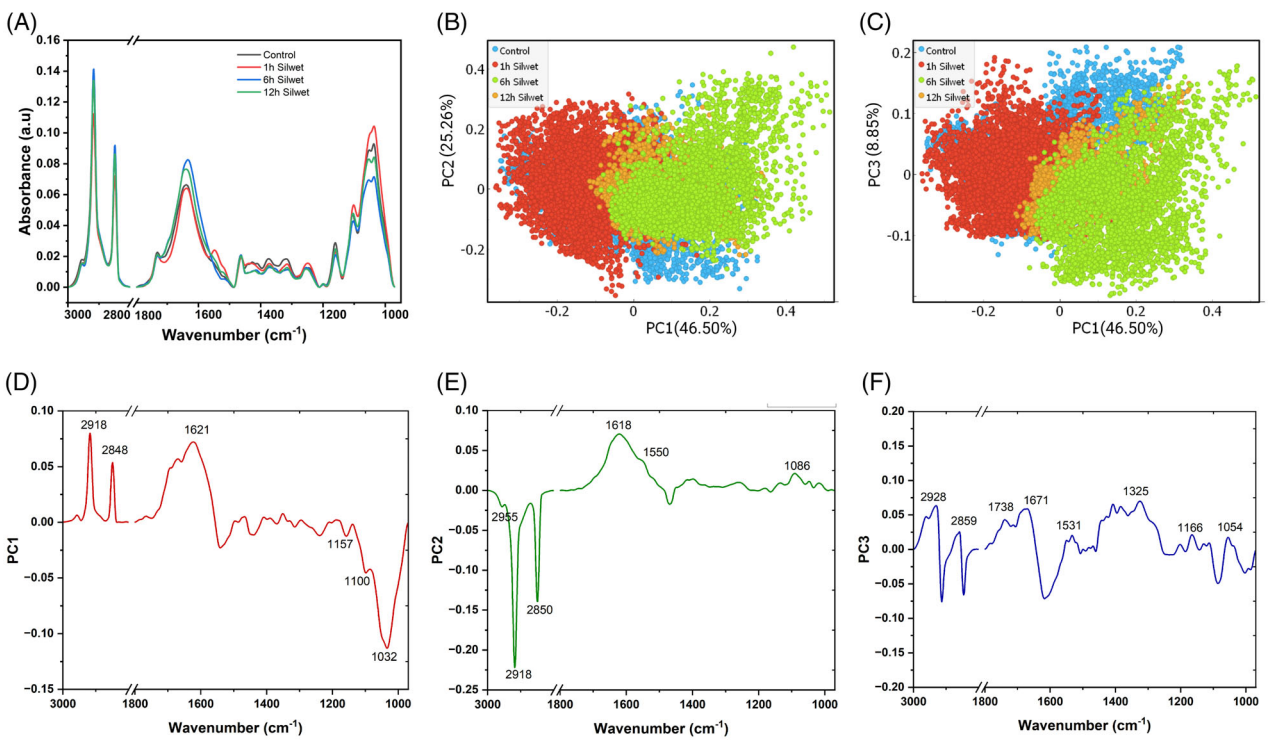

Figure 4. Overview of complete synchrotron macro-ATR-FTIR dataset using absorbance data.
(A) Average absorbance spectra of control and Silwet-L-77-treated leaves after 1, 6 and 12 h of application. PCA score plots (B, C) and loading plots (D–F) show differences in biochemical characteristics between control and surfactant-treated leaf samples.

three characteristic spectral regions that are particularly important for plant biological materials, including methyl and methylene groups (3000–2800 cm^{-1}) for lipids (Khambatta et al., 2021), amide I and II (1700–1500 cm^{-1}) for proteins (Baker et al., 2014) and fingerprint regions (1180–970 cm^{-1}) for carbohydrates (Kerr et al., 2013). Annotations of the peaks observed in the spectra collected from maize leaves are shown in Table 1.

Unsupervised multivariate principal component analysis (PCA) was performed to identify the similarities and differences between control and surfactant-treated leaves across different time points. PCA score and loading plots are presented in Figure 4B,C and 4D–F, respectively. The first three principal components explained 80.61% of the total variance in the original data (Figure 4B,C). Despite partial overlap between the control and Silwet-L-77-treated groups, greater separation between the 1 h post-treatment and later time points of 6 and 12 h suggests a time-dependent response of maize leaves to the application of surfactant. The strong loadings that appeared for both PC1 and PC2 are associated with the stretching of methyl/methylene of lipids (peaks located at 2955, 2918 and 2848/2850 cm^{-1}) and amide I protein structures (1621/1618 cm^{-1}). In addition, the PC1 loading plot shows strong peaks for carbohydrates (1157, 1100 and 1032 cm^{-1}) while the PC2 loading plot shows an additional peak for amide II (1550 cm^{-1}) (Figure 4D,E). The PC3 loading plot, which represents 8.85% of the data, showed peaks at 1738 and 1671 cm^{-1}, which correspond to C=O ester from lignin or pectin and amide I, respectively (Figure 4C,F).

In another approach, second derivatives were calculated and vector-normalized average second derivative spectra are shown in Figure 5A,B. The PCA score and loading plots of processed data after outlier removal are presented in Figure 5C–G. The first three components of the PCA represent 40.9% of the original data (Figure 5C,D). The PC1 loading showed a clear difference driven by lipid-related peaks (2922, 2913, 2854 and 2845 cm^{-1}) (Figure 5E). In the PC2 loading, aside from the peaks for the lipid-related region (for example, 2919 and 2851 cm^{-1}), peaks for carbohydrates appeared strongly at 1160, 1105, 1052, 1034 and 990 cm^{-1} and, in addition, the appearance of the peak in the protein regions which are located at 1734, 1652 and 1544 cm^{-1} (Figure 5F). Strong peaks appearing in the PC3 loading are similar to those in the PC2 loading with stronger peaks indicating the carbohydrates (for example, 1162, 1046, 1036 and 993 cm^{-1}) (Figure 5G).

In addition to PCA score and loading plots shown in Figures 4 and 5, PCA analysis based on the average spectra of each biological sample may be carried out to provide a more simplified version of the PCA analysis (Figure S2). A clearer separation between treatment groups and clustering of treatment replicates is shown, clearly demonstrating biochemical changes of the leaf surface with increasing surfactant exposure time.

False-color images (Figure 6) were generated by integrating the peak(s) in three major regions including: $\nu_s CH_2$ (2865–2835 cm^{-1}) for lipids, amide II (1572–1525 cm^{-1}) for proteins and carbohydrates (1180–970 cm^{-1}). The maize leaf cross-section consists of an outermost hydrophobic barrier made up of the epicuticular wax and the cuticle followed by the upper epidermis and mesophyll cells (Elliott et al., 2023). Pavement cells and stomata are the two major types of epidermal cells. The pavement cells were roughly rectangular with rounded vertices and wavy

Table 1 Annotation for typical peaks that appeared in the spectra collected from maize leaf. The references are those for which the peaks were identified and categorized.

Region	Peak	Band assignment	References
2965-2950	2955	Asymmetric CH_3 stretching from lipids	Liu et al. (2020)
2935-2895	2918	Asymmetric vibration of CH_2 from lipids	Khambatta et al. (2021)
2865-2835	2848	Symmetric vibration of CH_2 from lipids	Khambatta et al. (2021)
1750-1720	1734	C=O ester from lignin or pectin	Kerr et al. (2013)
1705-1565	1650	Amide I band including C=O stretching, N-H bending and C-N bending	Willick et al. (2018)
1572-1525	1544	Amide II band including N-H bending and C-N stretching	Guendel et al. (2018), Siriwong et al. (2022)
	1462	Asymmetric CH_3 and CH_2 bending from lipids, protein and lignin	Thumanu et al. (2017)
	1371	Symmetric CH_3 and CH_2 bending from lipids, protein and lignin	Cuello et al. (2020)
1270-1215	1248	C-O stretching from lignin and hemicelluloses	Kerr et al. (2013)
	1200	C–O–C from polysaccharides, cellulose, hemicellulose and pectin	Tanino et al. (2013)
	1160	C-C ring cellulose	Cuello et al. (2020)
1138-970	1100, 1050, 1032	C-O, C-C stretching from carbohydrates	Thumanu et al. (2017)

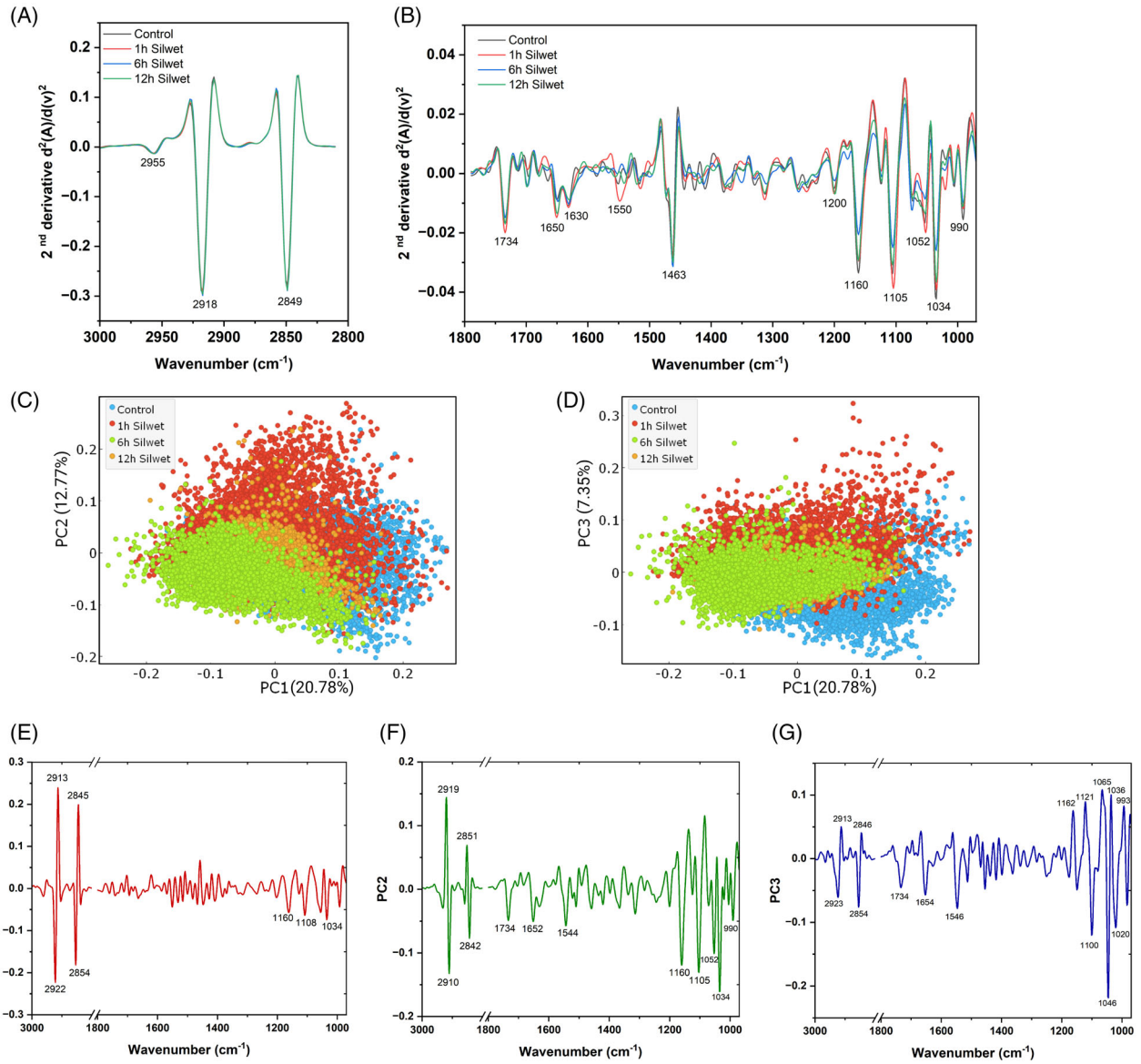

Figure 5. Overview of complete synchrotron macro-ATR-FTIR dataset using second derivative data.
(A, B) Average second derivative spectrum for each of control or surfactant-treated groups. PCA score plots (C, D) and loading plots (E–G) show differences in biochemical characteristics between control and surfactant-treated leaf samples.

outlines that are arranged in alternating rows parallel to the major vein of the leaf. The stomata usually share the same width as the pavement cells and are aligned with them in linear rows and these rows were distributed randomly across the leaf surface. In the false-color functional group images (Figure 6), the distribution of $\nu_s CH_2$, a characteristic marker for epicuticular waxes, closely corresponded with the morphology of individual pavement cells and stomata as observed in the bright field images of both control and Silwet-L-77-treated leaves. The distribution of $\nu_s CH_2$ in the control leaves highlighted the heterogeneous characteristics of epicuticular wax on the leaf surface that became more pronounced after the application of the surfactant. False-color functional group images of amide II revealed generally weak integrated peak intensities, as shown by the predominantly blue color of the images for the control as well as 6 and 12 h treated samples. However, a notably higher integrated peak intensity of amide II was observed for 1 h surfactant-treated leaves, particularly in regions corresponding to pavement cells. Carbohydrates were mapped using the characteristic broad region in the wavenumber range 1180–970 cm^{-1}, corresponding to C-O-C bonding, which was clearly distributed across the entire sample and did not distinguish

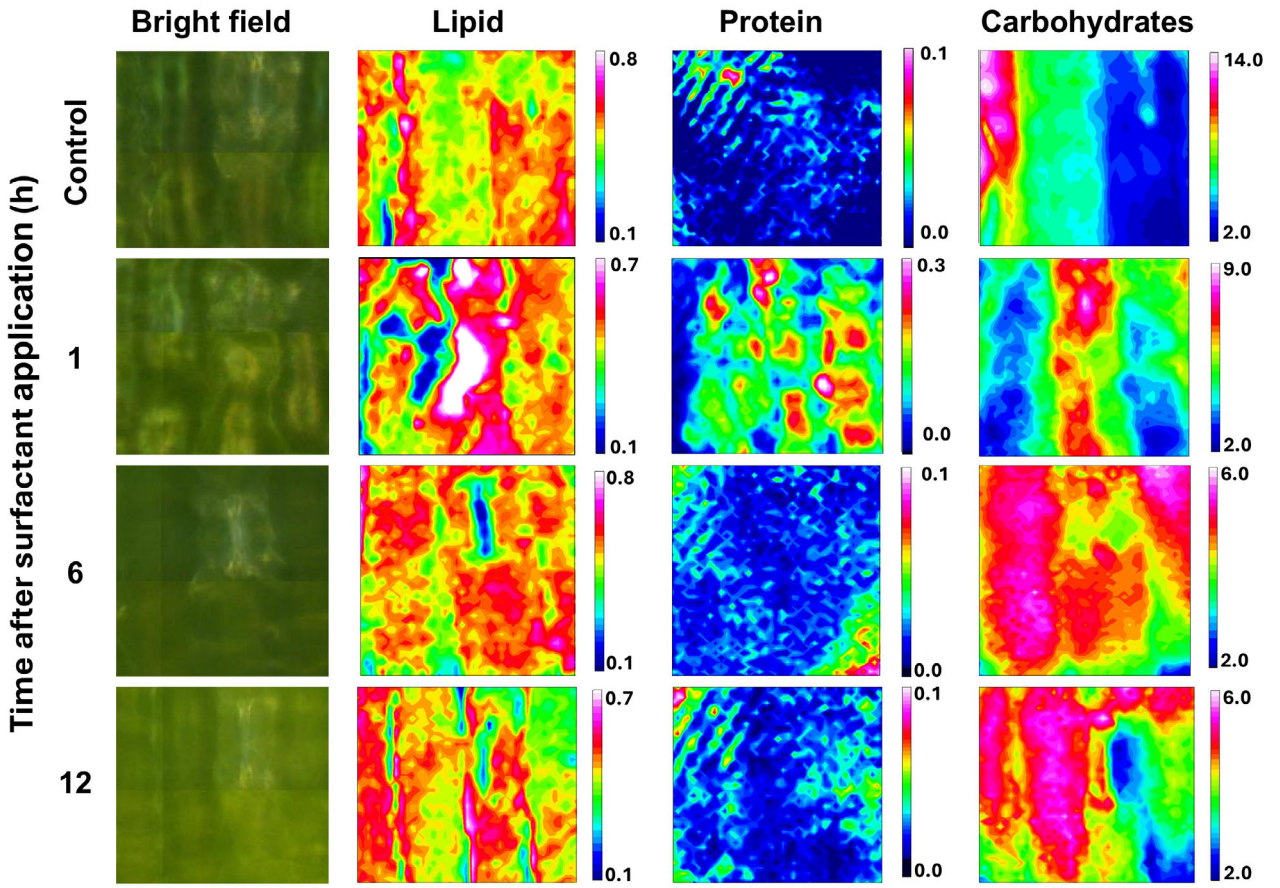

Figure 6. Representative bright-field images and high-resolution false-color chemical maps of control and 2% Silwet-L-77-treated maize leaves. Chemical maps were generated using the integrated peak areas of symmetric methylene (2865–2835 cm^{-1}) for lipids, amide II (1572–1525 cm^{-1}) for proteins and carbohydrates (1180–970 cm^{-1}). Each pixel corresponds to a single spectrum with approximately 1500 spectra comprising each chemical map.

between different pavement cells and stomata in either control or treated leaves.

The results of the data analysis using absorbance or second derivatives revealed similar insights into the changes in lipids, proteins and carbohydrates in the maize leaf treated with the surfactant. As calculated from the absorbance, the integrated peak areas for $\nu_{as}CH_3$ (2965–2950 cm^{-1}), $\nu_{as}CH_2$ (2935–2895 cm^{-1}) and ν_sCH_2 (2865–2835 cm^{-1}) showed a small but significant decrease at 1 h of Silwet-L-77 treatment (Figure S3a–c). However, these areas showed an increase at 6 and 12 h surfactant-treated leaves as compared with the control. The second derivative peaks of the corresponding regions including $\nu_{as}CH_3$ (2955 cm^{-1}), ν_sCH_2 (2918 cm^{-1}) and $\nu_{as}CH_2$ (2848 cm^{-1}) showed no changes or higher intensity in the treated leaves relative to the control (Figure S4a–c). Amide I region peak area (1705–1565 cm^{-1}) increased notably in leaves after 6 and 12 h of the surfactant treatments (Figure S3d). The same effects were observed in second derivatives with strong peaks located at 1650 and 1630 cm^{-1} in the amide I region (Figure S4d,e). These peaks were attributed to the α-helix and β-sheet secondary structures of proteins, respectively (Lahlali et al., 2014; Willick et al., 2018). Interestingly, both amide II peak area (1572–1525 cm^{-1}) and the secondary peak intensity of amide II at 1550 cm^{-1} indicated a significant increase at 1 h, which was not observed at 6 or 12 h after the application of the surfactant (Figure 6; Figures S3e and S4f). The rapid increase in the amide II absorbance peak area or peak intensity of second derivative of the 1 h surfactant-treated sample is likely to be associated with the quick response of the plant to the surfactant that might occur in a time-dependent manner. For carbohydrate peak area (1180–970 cm^{-1}), we observed a reduction in the 6 and 12 h treated leaves in comparison to the control (Figure S3f). Similarly, second derivative peak intensities at 1160, 1105, 1034 and 990 cm^{-1} associated with C-O and C-C stretching vibrations from carbohydrates, were lower in surfactant-treated samples in comparison to the control (Figure S4g–j).

DISCUSSION

The utilization of surfactants in agriculture has been documented for over 70 years (Stevens, 1993), highlighting their role in enhancing the spreading and wetting

properties of agrichemical formulations (Jibrin et al., 2020). However, the adverse effects of these surfactants on chemical alterations to plant leaves remain underexplored. Here, we used advanced synchrotron macro-ATR-FTIR for chemical mapping of major macromolecules to provide an assessment of a leaf after treatment with a commonly used surfactant. The outcome of this study is not only to reveal and provide more understanding of the interactions between surfactants and a leaf but also to demonstrate the potential of applying synchrotron macro-ATR-FTIR to plants to explore molecular changes during the interaction between plants and external stressors.

Surfactant effects on maize leaves can be quantified by contact angle measurement, SEM and PAM analyses

The contact angle of water droplets on the surface of the maize leaf was dramatically reduced when Silwet-L-77 was introduced into the solution, and this effect increased with increasing concentration. When wax platelets on the epicuticular layer are removed, as observed by SEM imaging, the contact angle is reduced. The surfactant in our study is a non-ionic organosilicon which has been shown to reduce the contact angle and thereby improve the deposition and spreading of the droplet in the leaf (Tang et al., 2008; Wagner et al., 1999; Zhang et al., 2006). For example, an increase in the uptake of fungicides in citrus (Srinivasan et al., 2008), pesticides or herbicides in wheat (Liu & Zabkiewicz, 1997) has been demonstrated for this surfactant. However, the application of surfactant in general at higher doses leads to phytotoxicity, for example, on tomato (*Solanum lycopersicum* L.) that were treated with four different surfactants at concentrations of 0.25–1.00 g/L (Liu & Stansly, 2000), or on peach (*Prunus persica* (L.) Batsch) treated with organosilicon surfactants (Fernández et al., 2008). Therefore, we further investigated whether the application of the surfactant affects the fundamental physiological process of the leaf by determining leaf photosynthetic performance based on the measurement of chlorophyll fluorescence.

The adverse effects of the higher concentrations of 0.2% and 2% were indicated by the decrease in values of ΦPSII and qP, while increasing the value of ΦNO which was shown after at least 6 h following treatment. The reduction in the effective quantum yield (ΦPSII) in treated leaves indicates that a lower proportion of absorbed light was used for photosynthesis. Instead, energy was being diverted to non-regulated dissipation processes, as evidenced by the increase in ΦNO. These changes are likely due to irreversible damage to the PSII reaction centres caused by the high concentration of the surfactant (Toscano et al., 2022). A study by Rasch et al. (2018) demonstrated that the surfactant polyoxyethylated tallow amine (POEA) irreversibly reduced the water permeability of the cuticle in kohlrabi (*Brassica oleracea* L.) leaves and impaired their photosynthetic capacity. In addition, we found that the coefficient of photochemical quenching (qP) value was reduced by the application of higher concentrations of the surfactant to the maize leaves. This indicates that there is a lower fraction of PSII reaction centres that are open and capable of photochemistry, as suggested by Zhao et al. (2024), demonstrating the possible impairment of the photosynthetic apparatus.

Advantages of synchrotron macro-ATR-FTIR in studying surfactant–leaf interactions

Although the physical mechanisms of surfactant interaction with leaf surfaces are well-studied, their detailed impacts on leaf molecular composition remain unclear. To investigate the alterations in the chemical composition of the plant surface including epicuticular waxes, cuticle and epidermal cells, liquid chromatography (LC–MS) or gas chromatography–mass spectrometry (GC–MS) techniques are considered standard analytical methods (Fernandez et al., 2016; Tran et al., 2023). Although these methods are widely used, as explained by Bourgault et al. (2020) extensive, destructive and time-consuming sample preparation with the use of hazardous organic solvents is generally required. In addition, the acquired information only reflects the average intrinsic properties of complex heterogeneous cells and there is limited capability to resolve biochemical changes at the subcellular and cellular levels.

In our study, we demonstrated that 2% Silwet-L-77 induced the most significant effects on the leaf surface and on photosynthetic performance. Therefore, we further investigated changes in macromolecular compositions of the leaf treated with this concentration of surfactant using high-resolution synchrotron macro-ATR-FTIR. We have demonstrated for the first time the application of this advanced technique to gain direct evidence for the spatial distribution of chemical functional groups within leaf cells treated with a surfactant. Mid-infrared microspectroscopy, as used here, allowed direct imaging of specific functional groups, both individually and in combination within a single experiment while localizing their distribution within cells. Although many of the molecules that are categorized as proteins, carbohydrates and lipids can be characterized individually, the interplay between these molecules and their distribution provides a more comprehensive understanding of the chemical processes that underlie complex biological systems.

To analyze infrared spectral data, multiple software and platforms are available, including CytoSpec (Cytospec Inc., Germany), OriginLab (OriginLab Corp., USA), OPUS (Bruker Corp., USA), MatLab (The MathWorks Inc., USA), the R language (R Foundation for Statistical Computing, Austria) and as used here, Quasar (open source, Toplak et al., 2017). Among these, Quasar stands out as a relatively new yet powerful platform, offering free access and

a user-friendly interface which requires no coding background to build a workflow and interactively explore analytical ideas. As such, Quasar workflows have only been used in a small number of studies. For example, Sandt et al. (2022) applied Quasar to analyze β-amyloid protein in bacterial cells, while Willick et al. (2020) demonstrated a basic workflow to investigate cold stress responses in *Triticum aestivum* L.. Here, we developed more comprehensive and detailed workflows along with specific examples and outcomes for data derived from and measured in plant leaves. These workflows enable exploration of FTIR data through diverse pathways such as data selection, unsupervised exploration, semi-quantitative analysis and spatial mapping, thereby providing a comprehensive understanding of plant biochemical responses to external treatments in a time-effective manner and making FTIR-based analysis more accessible to plant scientists.

The principle of ATR-FTIR is based on total internal reflection at the interface between an ATR crystal and the sample to generate an evanescent wave that penetrates the sample surface. The oscillating electric field of this wave interacts with the molecular dipoles in the biological sample and produces an infrared absorption spectrum that reveals its molecular composition (Baker et al., 2014; Morais et al., 2020). The depth of penetration of the synchrotron macro-ATR-FTIR used in this study varies around 0.2–5 μm (Vongsvivut et al., 2019). The anatomical structure of a typical mature maize leaf consists of an epicuticular wax layer with a height of a few nanometers (Nadiminti et al., 2015) and a cuticle layer of around 40 nm (Bourgault et al., 2020), while the thickness of the epidermal cell wall ranges from 2 μm to 6.8 μm (Sayad et al., 2023) (Figure 7B). This indicates that the penetration of the evanescent wave in contact with the maize leaf in this study would potentially penetrate the epidermal cell wall and plasma membrane (Figure 7C).

Lipid region analysis in our study showed that after 1 h of the Silwet-L-77 treatment, the absorbance peak area decreased while second derivative peak intensities showed no significant change. However, at 6 and 12 h post-treatment, both the peak area and second derivative intensities increased. As demonstrated by SEM in this study, the surfactant can cause changes to the morphology of the waxy epicuticular layer, but it is unlikely to break the chemical bonds of lipids in the cuticles. This could explain why lipid-related intensities are likely to not change at 1 h after surfactant application. However, a high concentration of surfactant can readily diffuse through the cuticle and into the underlying cells (Elliott et al., 2023) to cause disruption to the cell membrane (Baales et al., 2024; John et al., 1974). This disruption likely causes the leakage of intercellular lipids into the cuticle, resulting in the increase in lipids observed in treated samples at 6 and 12 h (Figure 7B).

Second-derivative peaks of amide I at 1650 and 1630 $cm,^{-1}$ which are associated with α-helix and β-sheet secondary structures of a protein, were higher in treated leaves than in the control at 6 and 12 h. Meanwhile, the amide II intensity only increased specifically at 1 h after the surfactant application. These effects of the surfactant on the leaf proteins are likely associated with early, stress-induced protein formation (at 1 h) followed by protein structural modifications due to ongoing stress (at 6 and 12 h), similar to the immediate and later responses of leaves to various environmental stressors, as described by Baales et al. (2024). The plant response to abiotic stress occurs in three major stages: (1) the 'stop phase,' characterized by a decreased growth rate, (2) the 'quiescent phase' where growth remains steady and (3) the 'recovery phase' during which growth resumes (Geng et al. 2013; Julkowska and Testerink 2015; Gallo et al., 2023). However, in our study, we found that the recovery phase does not occur in maize leaves treated with the higher surfactant concentrations of 0.2% and 2%, as shown by a reduction in photosynthesis-related parameters from 6 to 24 h after surfactant exposure.

Non-ionic surfactants containing ethoxylate groups interact with hydrophobic moieties of proteins, which might partially affect protein folding or aggregations if the surfactant concentration exceeds a certain threshold, typically above the critical micelle concentration (Aguirre-Ramirez et al., 2021; Otzen, 2011). Higher concentrations of surfactant can lead to the alteration of the proportion of various protein secondary structures in plants, as shown by the increase in the peak intensities for α-helices and β-sheets belonging to the amide I region, as shown in our study and others. Willick et al. (2018), for example, showed that concentrations of both α-helix and β-sheet structures increased in the shoot of winter wheat (*Triticum aestivum* L.) after 21 and 42 days of freezing stress. These changes were associated with the modification of ice binding sites of antifreeze proteins, as determined by LC–MS. Alterations in protein secondary structures can also be shown by a transition in the peak position of α-helices or β-sheets (Sharma & Uttam, 2016); for example, Yang and Yen (2002) reported a rapid increase in the ratio of α-helices to β-sheets (1680/1640 cm^{-1}) observed in Arabidopsis within 12 h of being exposed to salt stress. In contrast, Lahlali et al. (2014) showed a reduction in the intensity of α-helices or β-sheets in pea pollen (*Pisum sativum* L.) subjected to heat stress.

The rapid increase in the peak intensity assigned for amide II 1 h after treatment may be associated with the immediate response of plant leaves to remodel the cell membrane. For example, Gallo et al. (2023) found that the highest number of significantly up-regulated proteins (261 proteins) was detected in the shoots of Arabidopsis after 1 h exposure to osmotic stress, compared to later time

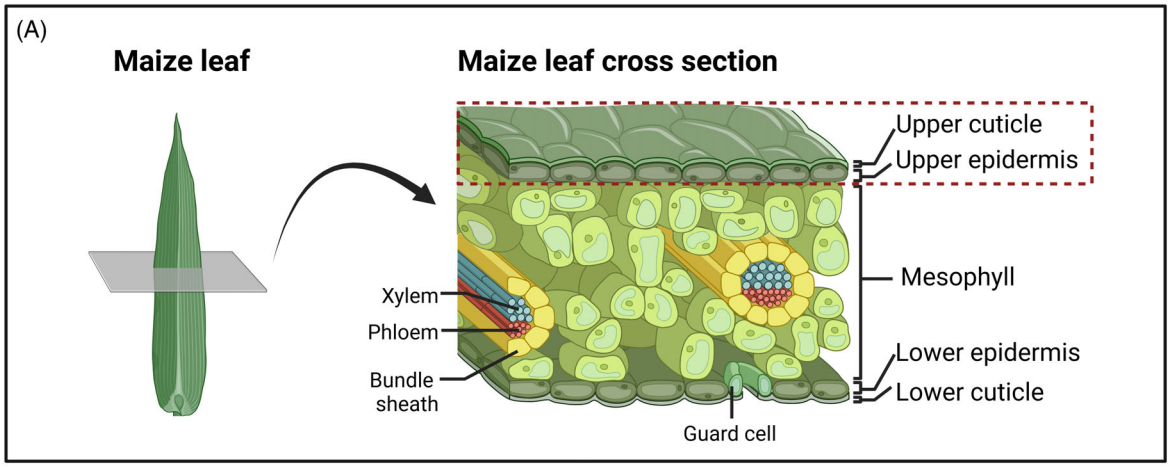

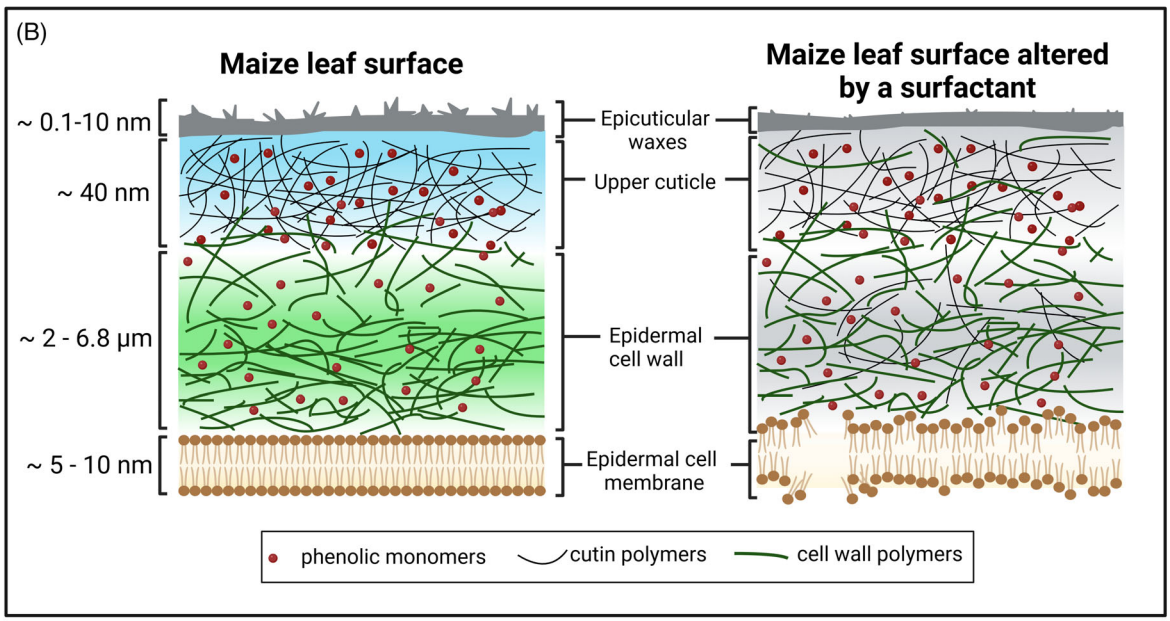

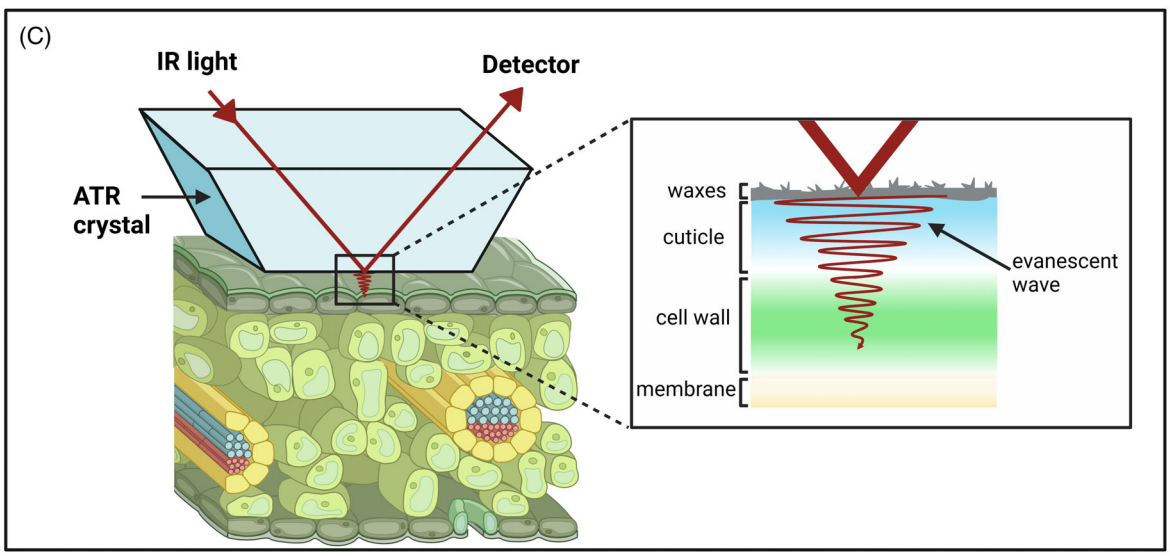

Figure 7. Diagrammatic structure of a maize leaf cross-section and the principle behind the synchrotron macro-ATR-FTIR technique.
(A) The maize leaf cross-section consists of an uppermost hydrophobic barrier made up by the epicuticular wax and the cuticle, below which are the upper epidermis and mesophyll cell layers. The vascular system including xylem and phloem is surrounded by bundle sheath cells.
(B) An expanded view of the epicuticular waxes, cuticle and epidermis layers before and after being treated with a surfactant at a relatively high concentration. Note that layers shown are for demonstration purposes and are not shown to scale. In the control leaf, the epicuticular layer containing wax platelets covers the cuticle, which consists of a dense cutin matrix and phenolic compounds. The underlying epidermal cell walls contain various polymers including cellulose, hemicellulose, lignin and pectin embedded with phenolic compounds. Following exposure to a surfactant, modification to the structure of the wax layer, cuticle, cell wall and cell membrane is likely to occur and to be associated with changes in FTIR signals.
(C) The working principle of synchrotron ATR-FTIR is based on total internal reflection at the interface between an ATR crystal and the sample to generate an evanescent wave that penetrates the sample surface. The depth of penetration of the synchrotron ATR-FTIR used in this study varied around 0.2–5 μm, likely penetrating to the epidermal cell wall.

points at 6, 12 and 24 h. One of the major protein groups contributing to this upregulation was found to be related to phospholipid biosynthesis processes. In another study, Berkowitz et al. (2021) reported for Arabidopsis after being exposed to short-term stressors (<3 h), the upregulation of tissue-specific genes that were involved in stomatal development, lipid and wax metabolism and synthesis that was required for both cuticle formation and epidermal cell growth.

Lower intensities of carbohydrate-related second derivative peaks (located at 1160, 1105, 1034 and 990 cm^{-1}) or absorbance peak area (1180–970 cm^{-1}) were found in the Silwet-treated leaves at all timepoints. These peaks are mainly associated with cell wall components including cellulose, hemicellulose and pectin (Cuello et al., 2020). In addition, the plant cell wall is composed of cellulose microfibrils embedded in a matrix of hemicelluloses, pectins and lignins (Lampugnani et al., 2018). Surfactants have been shown to disrupt the structure of the cell wall by interfering with the interactions between the major constituents, either through the solubilization of specific components, such as lignin as shown by Seo et al. (2011) or weakening the hydrogen bond network within the cellulose framework as demonstrated by Solhi et al. (2023).

In conclusion, we have demonstrated that synchrotron macro-ATR-FTIR can be used as a non-destructive and *in vivo* imaging and characterization technique to investigate the plant leaf surface and sub-surface cell layers. We also developed different workflows for FTIR data analysis using Quasar software as an open, free-access and interactive platform to enhance the effectiveness of the use of synchrotron macro-ATR-FTIR. Specifically, we have, for the first time, applied the synchrotron macro-ATR-FTIR to gain insight into the effects, over time, of a surfactant on leaf chemical compositions. The efficacy of the surfactant in enhancing chemical uptake was demonstrated by its impact on contact angle and alterations in wax morphology of a maize leaf surface. However, spatial FTIR spectra and chlorophyll fluorescence revealed that at higher concentrations of surfactant there are major impacts on photosynthetic capacity and chemical composition. Synchrotron macro-ATR-FTIR is a facile sample preparation method that enables the collection of detailed cell-specific data and should be used to analyze in detail various plant structures across multiple tissues and organs.

EXPERIMENTAL PROCEDURES

Plant growth and treatment with surfactant

Maize (*Zea mays* L.) seeds (Eden Seeds, Australia) were soaked in distilled (DI) water overnight. The seeds were then surface-sterilized in 80% ethanol for 2 min, followed by incubation in 10% bleach (sodium hypochlorite, Chem-Supply, Australia) containing 0.1% Triton X-100 (Sigma, Australia) for 15 min. The seeds were then rinsed four times with DI water, placed on two layers of wet paper towels and kept in the dark at 21°C for 3 days in a plant growth chamber (Thermoline Scientific, Australia).

After 3 days, the germinated seeds were transferred to pots containing autoclaved sand and supplied with full strength Hoagland's solution (Hoagland & Arnon, 1950) (~50 mL/pot) every 3 days for a period of 5 weeks. Silwet-L-77 (Phytotech Labs, Australia) solutions at concentrations of 0%, 0.02%, 0.2% and 2% were sprayed to run-off (~1.5 mL) on both upper (adaxial) and lower (abaxial) surfaces of the fifth leaf at the V8 stage (O'Keefe, 2009) of each plant by using a 20 mL spray bottle. After the application, leaf samples were collected at different time points, 0 h (immediately after spray), 1, 6, 12 and 24 h after treatment depending on the analysis to be performed. The leaf samples collected at the relevant time point(s) were subjected to the following analyses.

Water droplet behavior following surfactant treatments was assessed using contact angle and surface tension measurements

The contact angle of a droplet was determined by the sessile drop method using an Attension Theta Flow Optical Tensiometer (Biolin® Scientific, Sweden). A small section of control or treated fresh maize leaf (10 × 40 mm) was mounted on a glass slide using double-sided adhesive tape. Four micro-liters of water solution containing 0, 0.02, 0.2 and 2% of Silwet-L-77 were deposited on the adaxial side of the leaf using a 1 mL precision syringe (Hamilton, USA). The deposited sessile drop was captured by a high-speed built-in camera mounted in line with the sample, and the static contact angle was calculated using the OneAttension software (Biolin® Scientific, Sweden). The capture speed was set at 3 frames per sec for a duration of 7 sec. For each leaf, one contact angle measurement was carried out, and a total of 30 leaves were analyzed for each treatment. The surface tension of Silwet-L-77 was assessed at five concentrations including 0.002%, and was determined using the pendant drop method (Berry et al., 2015). Images of droplets were captured at a rate of 12 frames per sec for a total duration of 5 sec.

Morphological analysis of maize leaf surface using scanning electron microscopy

To investigate the impact of Silwet-L-77 on leaf surface morphology, a scanning electron microscope (Zeiss Supra 55P SEM, Zeiss, Australia; SEM) was used. The fifth leaf of maize at the V8 stage (O'Keefe, 2009) was sprayed with water or Silwet-L-77 at concentrations ranging from 0.02% to 2% (as described above). After 1 h of the application, one set of leaf samples was collected and designated as unwashed samples. Another set of treated leaf samples was rinsed once with DI water, dried with the adaxial surface face-up on absorbent paper, and designated as washed samples. For each sample, an approximately 60 × 60 mm leaf section was mounted onto aluminum stubs using 10 μL of conductive isopropanol-based colloidal graphite (Ted Pella Inc., USA). The samples were then dried at 50°C for 18 h in an oven. Subsequently, the samples were sputter-coated with a 5 nm layer of gold using an EM ACE600 Sputter Coater (Leica, Australia) and observed under the SEM at a low voltage of 3 kV.

Photosynthesis performance of maize as measured by chlorophyll fluorescence

The impact of various Silwet-L-77 concentrations on maize photosynthetic performance was examined using chlorophyll fluorescence measurements. These measurements were obtained by using an Imaging Pulse Amplitude Modulation (IMAGING-PAM) Mini version (Heinz Walz GmbH, Germany) that was operated via the ImagingWinGigE software version 2.47. The settings for the IMAGING-PAM Mini were as follows: measuring light intensity = 1 (frequency = 1); saturation pulse = 9; gain = 1; dumping = 2; red gain = 25; red intensity = 4; NIR intensity = 7; Fm factor = 1.055; F factor = 0.999.

Maize plants were dark-adapted for 30 min, and a 10 × 40 mm section from the middle of the maize leaf was cut and mounted on a piece of white heavy-weight paper using double-sided adhesive tape to provide a flat surface. Chlorophyll fluorescence measurements were captured from the adaxial side of the leaf. Two rectangular areas of interest (AOIs), each approximately 2.6 cm^2, were defined on either side of the blade to avoid the midrib of the leaf. First, the values of minimal and maximum fluorescence, F_0 and F_m, respectively, were determined by a high-intensity saturation pulse. Second, the samples were pre-illuminated for 3 min with actinic light at low intensity (48 μmol/m^2/sec) to allow sufficient time for electron transfer through to the carbon cycle before a rapid light curve measurement was initiated. Finally, the rapid light curve with increasing actinic light steps (0, 23, 43, 81, 111, 145, 180, 269, 321 and 403 μmol/m^2/sec) with 30 sec intervals was applied. Photosynthetic parameters were obtained for leaves from each treatment group sprayed with 0%, 0.02%, 0.2% and 2% Silwet-L-77 at 1, 6, 12 and 24 h after treatment. At each timepoint, a total of five leaves were measured for each treatment group. A previous study by Ferguson et al. (2023) has shown that there is no significant difference in photosynthetic performances between intact and detached leaves, including those of maize, over a short period of time, such as overnight.

Synchrotron macro attenuated total reflectance-Fourier transform infrared (synchrotron macro-ATR-FTIR) microspectroscopy imaging of the maize leaf following surfactant treatment

Five-week-old leaves sprayed with DI water as the control or 2% Silwet-L-77 were collected after 1, 6, or 12 h after treatment. A small leaf section (approximately 10 × 10 mm) was cut and mounted on a CaF_2 disc fixed onto an aluminum disc and then placed into the microscope stage of the synchrotron macro-ATR-FTIR unit. FTIR hyperspectral data were collected via the infrared microspectroscopy (IRM) beamline at the Australian Synchrotron (Victoria, Australia) using the in-house developed macro-ATR accessory (Vongsvivut et al., 2019) with a Ge hemisphere (250 μm sensing facet). The beamline was equipped with a Vertex 80v spectrometer (Bruker), Hyperion 3000 microscope (Bruker, Australia) with a 20× objective (NA = 0.6) and mercury cadmium telluride (MCT) narrowband detector (50 μm element), using synchrotron radiation as the light source. The interferometer scanning velocity was 40 kHz with a KBr beamsplitter. The Fourier transform was subject to a Blackman-Harris 3-term apodization function and a zero-filling factor of two. FTIR hyperspectral maps were collected across the range 3900–750 cm^{-1} using a 2.5 μm projected aperture to restrict the beam. A large overview map (100 × 100 μm) was first collected to ensure good contact between the Ge crystal and the sample (background in air, 256 co-added scans) using 4 co-added scans and a step size of 5 μm in x- and y-directions. A second, higher quality map was then collected on a selected area within the overview map, using either 16 or 32 co-added scans and a step size of 2 μm in *x*- and *y*-directions.

Synchrotron macro-ATR-FTIR data analysis and the use of Quasar software

An approximately 40 × 40 μm high-resolution map was obtained for each of the control or surfactant-treated samples at different time points after the application of surfactant. Three biological replicates were included for each treatment group, except the 12 h Silwet-L-77-treated sample for which a single sample was analyzed. The total number of hyperspectra (or pixels) obtained for the control, 1, 6 and 12 h post-treatment groups was 3916, 4693, 3395 and 1597, respectively. Although only one maize sample was measured for the 12 h Silwet-L-77-treated group, the number of spectra was deemed sufficient to perform statistical analysis.

Synchrotron macro-ATR-FTIR data was subjected to atmospheric correction to eliminate any interference from water vapor and CO_2 in the atmosphere. This process was carried out using the OPUS software version 8.0 (Bruker Corp., USA). The data were then loaded into Quasar software version 1.7.2 (open source, Toplak et al., 2017) for further analysis. In Quasar, a workflow consists of various widgets, each defined as a component that performs specific functions, such as data processing, visualization, or modeling. In this study, we employ and describe two distinct approaches for data analysis utilizing absorbance and second derivative data. Details for the workflows and examples of results are provided in Figure 8–9 and Figures S5–S10.

Quasar workflow development

Absorbance data analysis

FTIR data was loaded into Quasar using a 'multiple files' widget and the sample name was defined using an 'edit domain' widget (Figure 8A; Figure S5). To eliminate any low-quality spectral data, data filtering was performed by applying a threshold of greater than 0.2 for the integrated peak area of ν_sCH_2 (2865–2835 cm^{-1}) in the lipid region, which is one of the most pronounced peaks in a typical plant spectrum collected from a leaf sample. The 'selected row' widget was used to collect the filtered data prior to data preprocessing. All samples were classified into different classes or treatment groups, including control, 1, 6 and 12 h after surfactant application using a 'create class' widget (Figure 8A; Figure S5). Data in the regions 3000–2800 cm^{-1} and

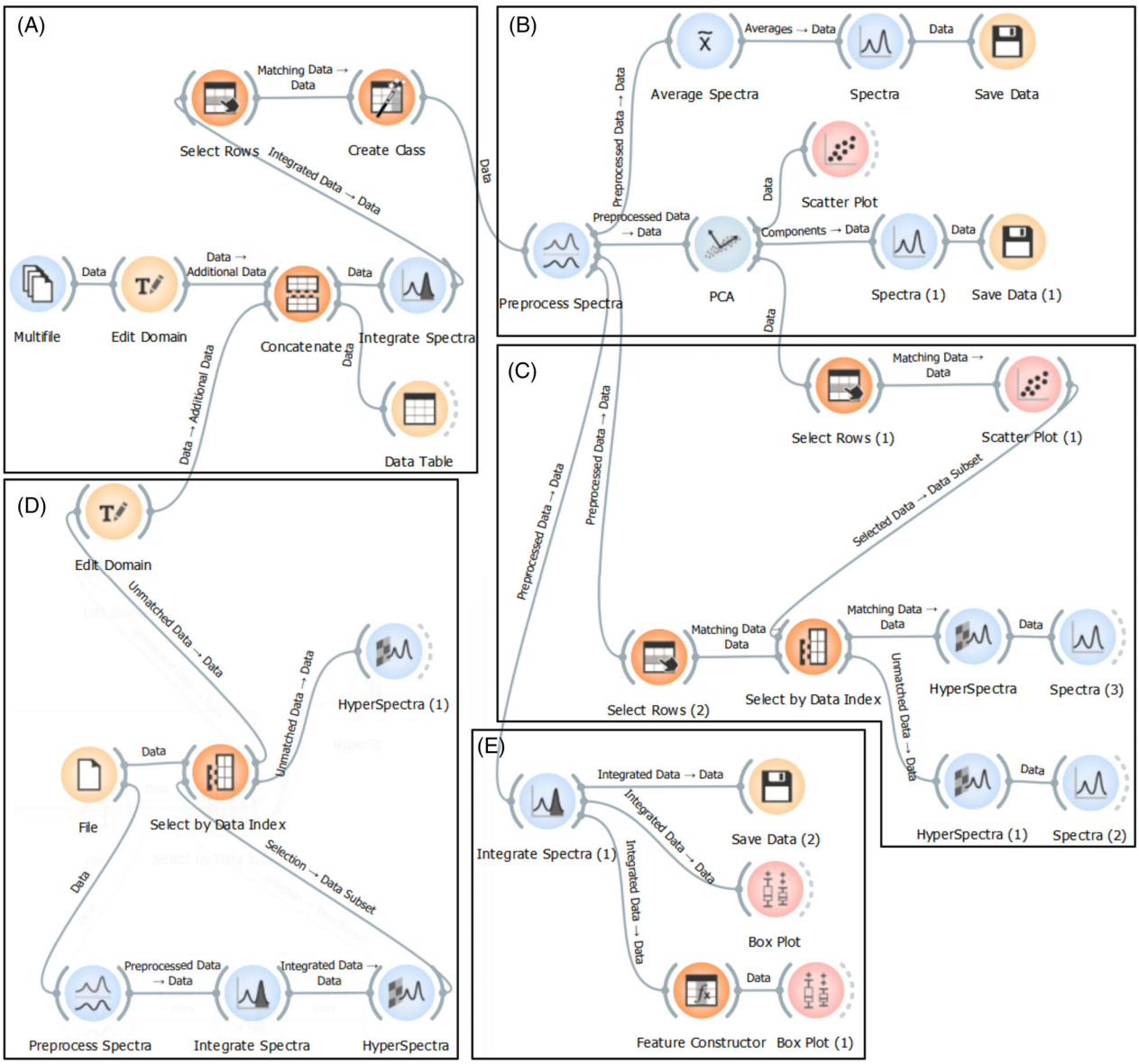

Figure 8. A Quasar workflow for analysis, visualization and extraction of hyperspectral synchrotron ATR-FTIR data obtained from leaf samples using absorbance data.
(A) Uploading, combining multiple data files and filtering data. Multiple data files were combined into a single dataset and filtered to eliminate any low-quality spectral data by applying a threshold of greater than 0.2 for integrated peak area of $\nu_s CH_2$ (2865–2835 cm^{-1}) in the lipid region.
(B) Data preprocessing, average absorbance spectra generation and unsupervised principal component analysis. Data in the regions 3000–2800 cm^{-1} and 1800–970 cm^{-1} was pre-processed, including baseline correction using a rubber band method and smoothing with a Savitzky–Golay filter. Average spectra for each treatment group, PCA score plot and loading plot were generated.
(C) Using PCA to identify variability among spectra obtained from the same leaf sample. The PCA score plot for each sample was analyzed to assess variability by examining how data points, each representing a spectrum, were distributed. Hyperspectral maps and absorbance spectra of the selected points from a PCA score plot were used to identify the sources of variation.
(D) A workflow used to upload a file separately and remove unwanted spectra based on hyperspectral maps.
(E) Workflow used to calculate integrated peak areas and visualize the results using box plots. Further details and examples for each of the workflows in this figure are provided in Figure S5–S9.

1800–970 cm^{-1}, where the major signals for biomolecules occur, were extracted and utilized in the subsequent preprocessing step. The effect of baseline drift was eliminated using rubber band baseline correction, followed by smoothing the data with a Savitzky–Golay (SG) filter (window size = 15, polynomial degree = 3) and vector normalization (Figure 8B; Figure S6). Average absorbance spectra for each treatment group were calculated using the 'average spectra' widget and visualized with the 'spectra' widget. Unsupervised analysis such as principal component analysis (PCA) can be performed to obtain an overview of the

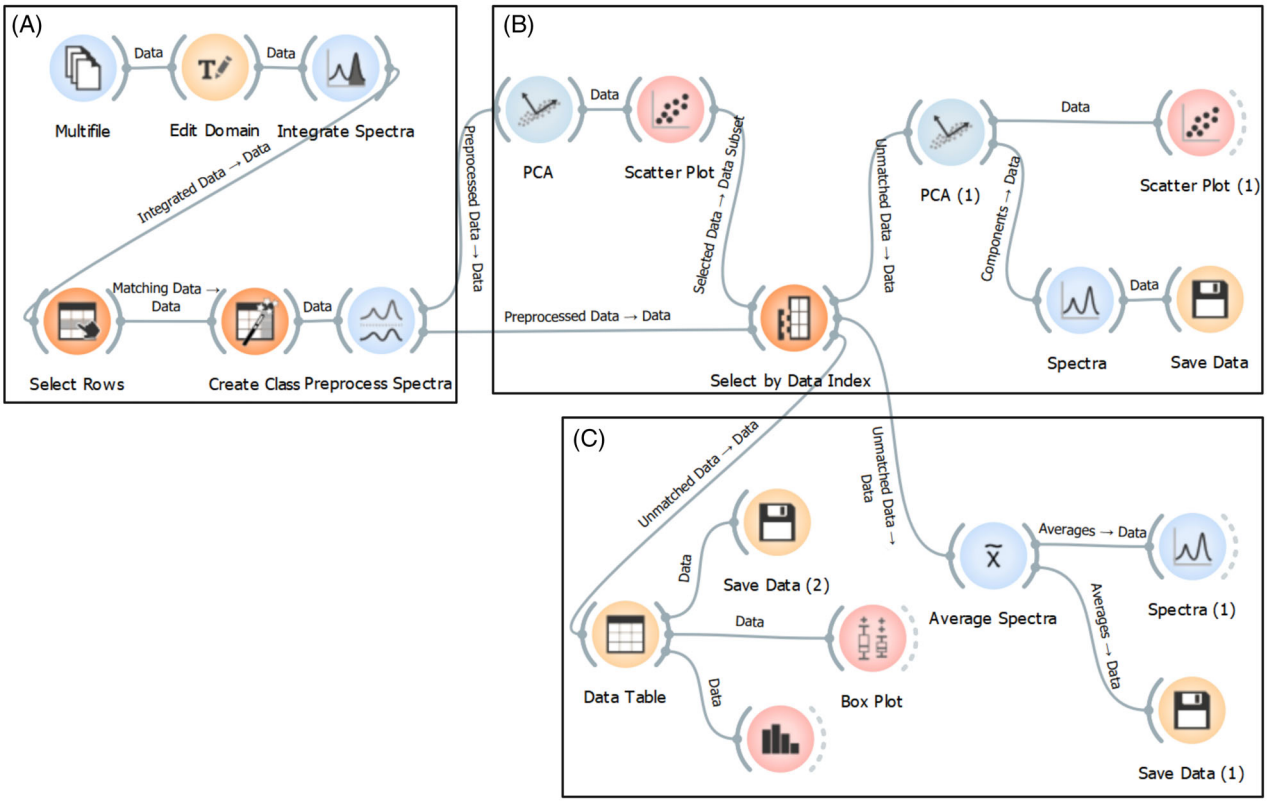

Figure 9. Quasar workflow for synchrotron ATR-FTIR data analysis based on second derivatives.
(A) Data was uploaded and filtered using the same threshold as in the workflow for the absorbance data as shown in Figure 8. Second derivatives of data in the regions 3000–2800 cm^{-1} and 1800–970 cm^{-1} were calculated by the Savitzky–Golay algorithm and normalized by vector normalization.
(B) PCA analysis to remove outliers and explore the differences between treatment groups.
(C) Average second derivative spectra for each treatment group were generated. Box plot and distribution plot can be used to examine any specific peak of interest. Further details and examples for each of the workflows in this figure are provided in Figure S10.

variability between control and surfactant treatment groups. The PCA score plot, where each data point represents a single spectrum, is used to identify clustering or separation of spectra from different treatment groups. Also, the spectral variance can be shown using a PCA loading plot that plots the principal components of the data (Figure S6c).

In this study, PCA was utilized not only to identify similarities and differences between control and surfactant-treated groups (Figure S6) but also to examine variability among spectra within the same sample of a treatment group (Figure 8C; Figure S7). Taking advantage of Quasar allowed any displayed data to remain accessible for further analysis, therefore, from selected points of the PCA score plot, hyperspectral maps and absorbance spectra can be generated to identify sources of variation (Figure S7). The 'select data index' widget enabled the extraction of specific spectral data from the original dataset that corresponded to outliers or manually selected points in the PCA score plot. In our study, due to the focus on the epidermis and cuticle layers of the leaf, we removed the spectra associated with the vein region from the dataset. A workflow as shown in Figure 8D was used to remove unwanted spectra based on a hyperspectral chemical map. Further explanation is provided in Figure S8.

After processing the data, peak integration can be performed for specific peaks of interest to facilitate comparisons between treatment groups. The integrated peak areas can be visualized using a box plot, which also displays the statistical significance of differences as determined by an ANOVA test (Figure 8E; Figure S9). In addition to calculating individual peak areas, the ratio of peak areas between different spectral regions is determined using the 'Feature Constructor' widget.

Second derivative analysis

Spectral absorbance data provides a general profile of the sample molecular composition, which is useful for the identification of spectral chemical features such as lipid, protein, or carbohydrates in this study. Absorbance data is also used to provide a direct correlation to the chemical concentrations (Morais et al., 2020). However, to enhance peak resolution and uncover subtle spectral features that may not be apparent in the original absorbance spectra, second derivative analysis can be applied. The Quasar workflow for this approach is provided in Figure 9 and Figure S10. Original absorbance data was input and filtered by applying a threshold for $\nu_s CH_2$, which is a similar method to the absorbance-based workflow as described above. For the next step of data preprocessing, second derivatives were calculated using the Savitzky–Golay filter (window size = 15, polynomial degree = 3, derivative order = 2) and then normalized using vector normalization (Figure 9A). PCA analysis was initially performed to remove outliers based on the clustering of each treatment group (Figure S10a,b). PCA was applied on the final dataset and the corresponding score and loading plots were generated (Figure 9B).

Average processed second derivative spectra for each treatment group can be displayed and extracted (Figure 9B). Further analysis, such as generating box plots and distribution plots for a second derivative peak, such as the amide II peak at 1550 cm^{-1}, can also be carried out (Figure 9C; Figure S10c).

All final analyzed data in Quasar were exported for visualization in Origin software version 2022b and GraphPad Prism version 10.2.2.

Statistical analysis

One-way ANOVA was performed to compare the means of a single variable between control and surfactant-treated samples (see Figure S3). Two-way ANOVA was performed to compare means of different treatments across various time points for photosynthesis (see Figure 3). Tukey's post hoc tests were used to compare means of each treatment group.

AUTHOR CONTRIBUTIONS

TT, DC, WY, YW and LK conceptualized and designed the project. TT performed the laboratory work, analyzed the FTIR data, wrote and revised the manuscript. JV and AK contributed to data acquisition and advised on data processing. TT, WY, DC, LK, YW, AK and JV contributed to the manuscript draft. WY and DC supervised and provided final approval of the manuscript. All authors approved the final version to be published and agreed with all aspects of the work.

ACKNOWLEDGMENTS

All authors gratefully acknowledge access to the Infrared Microspectroscopy (IRM) beamline at the Australian Synchrotron, infrastructure of the Australian Nuclear Science and Technology Organization (ANSTO) funded by the Australian Government. TT, WY, DC, YW and LK acknowledge the financial support provided by the Australian Research Council (ARC) Discovery scheme (DP220102729). Open access publishing facilitated by Deakin University, as part of the Wiley - Deakin University agreement via the Council of Australian University Librarians.

CONFLICT OF INTEREST

The authors declare no conflict of interest.

DATA AVAILABILITY STATEMENT

All relevant data can be found within the manuscript and its supporting information. Raw data are available from the corresponding author upon request.

SUPPORTING INFORMATION

Additional Supporting Information may be found in the online version of this article.

Figure S1. Chlorophyll fluorescence parameters using rapid light curves 24 h after treatment of maize leaves with Silwet-L-77. (a) ΦPSII, PSII effective quantum yield; (b) ΦNPQ, quantum yield of regulated energy dissipation; (c) ΦNO, quantum yield of non-regulated energy dissipation; (d) NPQ, non-photochemical quenching; (e) qN, coefficient of non-photochemical quenching (lake model, collective energy dissipation across interconnected PSII units); (f) qP, coefficient of photochemical quenching (puddle model, each PSII unit is independent with absorbed energy remaining localized); (g) qL, coefficient of photochemical quenching (lake model). Bars represent standard deviation of the mean ($n = 5$). Note that chlorophyll fluorescence parameters have no units, as they are typically expressed as ratios.

Figure S2. PCA score plots generated using the averaged absorbance spectra (a–b) and averaged second-derivative spectra (c, d) of each biological sample.

Figure S3. Peak areas for lipid (a–c), protein (d, e) and carbohydrate-related regions (f) for control and Silwet-L-77–treated leaves at different time points after application (1 h, 6 h and 12 h). Data are presented as mean values and error bars indicate the standard deviation (SD). Statistical analysis was performed using a one-way ANOVA followed by the post hoc Tukey's HSD test. Different letters above error bars indicate significant differences ($P < 0.05$) between samples.

Figure S4. Second derivative peak intensities for lipid (a–c), protein(d–f) and carbohydrates (g-j) in control and Silwet-L-77-treated leaves at different time points after application (1 h, 6 h and 12 h). Data are presented as mean values and error bars indicate the standard deviation (SD). Statistical analysis was performed using a one-way ANOVA followed by the post hoc Tukey's HSD test. Different letters above error bars indicate significant differences ($P < 0.05$) between samples.

Figure S5. Quasar workflow for uploading, combining multiple data files and filtering data. (a) Rename the sample name. (b) Combine multiple data files into a single dataset. (c) An example of combined data table to illustrate the dataset structure. (d) Filter the data to eliminate any low-quality spectral data with an integrated peak area for ν_sCH_2 (2865–2835 cm^{-1}) in the lipid region that is below 0.2.

Figure S6. Quasar workflow for data preprocessing, average absorbance spectra generation and unsupervised principal component analysis. (a) Data in the regions 3000–2800 cm^{-1} and 1800–970 cm^{-1} was pre-processed, including baseline correction using a rubber band method, smoothing with a Savitzky–Golay filter and vector normalization. (b) Average spectra for each treatment group. (c) Results of PCA score plots and loading plots to identify similarities and differences between treatment groups.

Figure S7. Using PCA to identify variability among spectra from the same sample. (a) PCA score plots for each of the three samples in the 1 h post-surfactant-treated group. (b) Spatial distribution in the hyperspectral map of selected points from 'sample 1' PCA score plot. (c) Absorbance spectra of the selected points from 'sample 1' PCA score plot and the remaining data in 'sample 1' after excluding these selected spectra.

Figure S8. Workflow used to upload a file separately and remove unwanted spectra based on hyperspectral maps. (a) Data from sample 1 was uploaded and pre-processed. (b) A hyperspectral map for the spatial distribution of carbohydrate region (integrated peak area in the 1180–970 cm^{-1}). (c) Bright field images of sample 1. (d) Chemical maps for carbohydrate region after removing the spectra in the secondary vein region.

Figure S9. Workflow used to calculate integrated peak areas and visualize the results using box plots. (a) An example of a box plot showing the peak area for the symmetric CH_2 stretch (ν_sCH_2) integrated within the region 2865–2835 cm^{-1}. (b) An example of a box plot showing the ratio between the asymmetric CH_3 and CH_2 peaks.

Figure S10. Workflow used to calculate second derivatives. (a) after filtering data, second derivatives were calculated by using the Savitzky–Golay (SG) filter followed by vector normalization. (b) PCA analysis was applied to remove outliers and identify

spectral differences between treatment groups (c) Examples of the box plot and distribution of a second derivative peak, such as amide II peak at 1550 cm^{-1}.

REFERENCES

Aguirre-Ramirez, M., **Silva-Jimenez, H.**, **Banat, I.M.** & **Diaz De Rienzo, M.A.** (2021) Surfactants: physicochemical interactions with biological macromolecules. *Biotechnology Letters*, **43**, 523–535.

Appah, S., **Jia, W.**, **Ou, M.**, **Wang, P.** & **Asante, E.A.** (2020) Analysis of potential impaction and phytotoxicity of surfactant-plant surface interaction in pesticide application. *Crop Protection*, **127**, 104961.

Baales, J., **Zeisler-Diehl, V.V.**, **Kreszies, T.**, **Klaus, A.**, **Hochholdinger, F.** & **Schreiber, L.** (2024) Transcriptomic changes in barley leaves induced by alcohol ethoxylates indicate potential pathways of surfactant detoxification. *Scientific Reports*, **14**, 4535.

Baales, J., **Zeisler-Diehl, V.V.**, **Malkowsky, Y.** & **Schreiber, L.** (2021) Interaction of surfactants with barley leaf surfaces: time-dependent recovery of contact angles is due to foliar uptake of surfactants. *Planta*, **255**, 1.

Baker, M.J., **Trevisan, J.**, **Bassan, P.**, **Bhargava, R.**, **Butler, H.J.**, **Dorling, K.M.** ***et al.*** (2014) Using Fourier transform IR spectroscopy to analyze biological materials. *Nature Protocols*, **9**, 1771–1791.

Barthlott, W., **Neinhuis, C.**, **Cutler, D.**, **Ditsch, F.**, **Meusel, I.**, **Theisen, I.** ***et al.*** (1998) Classification and terminology of plant epicuticular waxes. *Botanical Journal of the Linnean Society*, **126**, 237–260.

Berkowitz, O., **Xu, Y.**, **Liew, L.C.**, **Wang, Y.**, **Zhu, Y.**, **Hurgobin, B.** ***et al.*** (2021) RNA-seq analysis of laser microdissected *Arabidopsis thaliana* leaf epidermis, mesophyll and vasculature defines tissue-specific transcriptional responses to multiple stress treatments. *The Plant Journal*, **107**, 938–955.

Berry, J.D., **Neeson, M.J.**, **Dagastine, R.R.**, **Chan, D.Y.** & **Tabor, R.F.** (2015) Measurement of surface and interfacial tension using pendant drop tensiometry. *Journal of Colloid and Interface Science*, **454**, 226–237.

Bourgault, R., **Matschi, S.**, **Vasquez, M.**, **Qiao, P.**, **Sonntag, A.**, **Charlebois, C.** ***et al.*** (2020) Constructing functional cuticles: analysis of relationships between cuticle lipid composition, ultrastructure and water barrier function in developing adult maize leaves. *Annals of Botany*, **125**, 79–91.

Castro, M.J.L., **Ojeda, C.** & **Cirelli, A.F.** (2013) Advances in surfactants for agrochemicals. *Environmental Chemistry Letters*, **12**, 85–95.

Chen, H., **Yang, L.**, **Wu, P.**, **Liu, P.**, **Xu, H.** & **Zhang, Z.** (2024) Combined application of surfactants and iron-based metal–organic framework nanoparticles for targeted delivery of insecticides. *Chemical Engineering Journal*, **488**, 1–16.

Congreve, M. & Cameron, J. (Eds.). (2019) *Adjuvants - Oils, surfactants and other additives for farm chemicals used in grain production - Revised 2019 edition*. ACT, Australia: Grains Research & Development Corporation.

Cuello, C., **Marchand, P.**, **Laurans, F.**, **Grand-Perret, C.**, **Laine-Prade, V.**, **Pilate, G.** ***et al.*** (2020) ATR-FTIR microspectroscopy brings a novel insight into the study of Cell Wall chemistry at the cellular level. *Frontiers in Plant Science*, **11**, 105.

Demsar, J., **Curk, T.**, **Erjavec, A.**, **Gorup, C.**, **Hocevar, T.**, **Milutinovic, M.** ***et al.*** (2013) Orange: data mining toolbox in python. *Journal of Machine Learning Research*, **14**, 2349–2353.

Elliott, J.R., **Cortvriend, J.**, **Depietra, G.**, **Brennan, C.** & **Compton, R.G.** (2023) Kinetics of lipophilic pesticide uptake by living maize. *ACS Agricultural Science & Technology*, **3**, 445–454.

Ferguson, J.N., **Jithesh, T.**, **Lawson, T.** & **Kromdijk, J.** (2023) Excised leaves show limited and species-specific effects on photosynthetic parameters across crop functional types. *Journal of Experimental Botany*, **74**, 6662–6676.

Fernandez, V., **Bahamonde, H.A.**, **Javier Peguero-Pina, J.**, **Gil-Pelegrin, E.**, **Sancho-Knapik, D.**, **Gil, L.** ***et al.*** (2017) Physico-chemical properties of plant cuticles and their functional and ecological significance. *Journal of Experimental Botany*, **68**, 5293–5306.

Fernández, V., **Del Río, V.**, **Pumariño, L.**, **Igartua, E.**, **Abadía, J.** & **Abadía, A.** (2008) Foliar fertilization of peach (*Prunus persica* (L.) Batsch) with different iron formulations: effects on re-greening, iron concentration and mineral composition in treated and untreated leaf surfaces. *Scientia Horticulturae*, **117**, 241–248.

Fernandez, V., **Gil-Pelegrin, E.** & **Eichert, T.** (2021) Foliar water and solute absorption: an update. *The Plant Journal*, **105**, 870–883.

Fernandez, V., **Guzman-Delgado, P.**, **Graca, J.**, **Santos, S.** & **Gil, L.** (2016) Cuticle structure in relation to chemical composition: Re-assessing the prevailing model. *Frontiers in Plant Science*, **7**, 427.

Gallo, R.M.C., **Li, Q.**, **Talasila, M.** & **Uhrig, R.G.** (2023) Quantitative time-course analysis of osmotic and salt stress in *Arabidopsis thaliana* using short gradient multi-CV FAIMSpro BoxCar DIA. *Molecular and Cellular Proteomics*, **22**, 100638.

Geng, Y., **Wu, R.**, **Wee, C.W.**, **Xie, F.**, **Wei, X.**, **Chan, P.M.** ***et al.*** (2013) A spatio-temporal understanding of growth regulation during the salt stress response in Arabidopsis. *The Plant Cell*, **25**, 2132–2154.

Guendel, A., **Rolletschek, H.**, **Wagner, S.**, **Muszynska, A.** & **Borisjuk, L.** (2018) Micro imaging displays the sucrose landscape within and along its allocation pathways. *Plant Physiology*, **178**, 1448–1460.

Hoagland, D.R. & **Arnon, D.S.** (1950) The water culture method for growing plants without soil. *California Agricultural Experiment Station*, **347**, 32.

Hu, X., **Gong, H.**, **Liu, H.**, **Wang, X.**, **Wang, W.**, **Liao, M.** ***et al.*** (2022) Contrasting impacts of mixed nonionic surfactant micelles on plant growth in the delivery of fungicide and herbicide. *Journal of Colloid and Interface Science*, **618**, 78–87.

Jibrin, M.O., **Liu, Q.**, **Jones, J.B.** & **Zhang, S.** (2020) Surfactants in plant disease management: a brief review and case studies. *Plant Pathology*, **70**, 495–510.

John, J.S., **Bartels, P.** & **Hilton, J.** (1974) Surfactant effects on isolated plant cells. *Weed Science*, **22**, 233–237.

Julkowska, M.M. & **Testerink, C.** (2015) Tuning plant signaling and growth to survive salt. *Trends Plant Science*, **20**, 586–594.

Kerr, J.L., **Baldwin, D.S.**, **Tobin, M.J.**, **Puskar, L.**, **Kappen, P.**, **Rees, G.N.** ***et al.*** (2013) High spatial resolution infrared micro-spectroscopy reveals the mechanism of leaf lignin decomposition by aquatic fungi. *PLoS One*, **8**, e60857.

Khambatta, K., **Hollings, A.**, **Sauzier, G.**, **Sanglard, L.**, **Klein, A.R.**, **Tobin, M.J.** ***et al.*** (2021) "Wax on, wax off": in vivo imaging of plant physiology and disease with Fourier transform infrared reflectance microspectroscopy. *Advanced Science*, **8**, e2101902.

Lahlali, R., **Jiang, Y.**, **Kumar, S.**, **Karunakaran, C.**, **Liu, X.**, **Borondics, F.** ***et al.*** (2014) ATR-FTIR spectroscopy reveals involvement of lipids and proteins of intact pea pollen grains to heat stress tolerance. *Frontiers in Plant Science*, **5**, 747.

Lampugnani, E.R., **Khan, G.A.**, **Somssich, M.** & **Persson, S.** (2018) Building a plant cell wall at a glance. *Journal of Cell Science*, **131**, jcs207373.

Liu, N., **Zhao, L.**, **Tang, L.**, **Stobbs, J.**, **Parkin, I.**, **Kunst, L.** ***et al.*** (2020) Mid-infrared spectroscopy is a fast screening method for selecting Arabidopsis genotypes with altered leaf cuticular wax. *Plant, Cell & Environment*, **43**, 662–674.

Liu, T.-X. & **Stansly, P.A.** (2000) Insecticidal activity of surfactants and oils against silverleaf whitefly (*Bemisia argentifolii*) nymphs (Homoptera: Aleyrodidae) on collards and tomato. *Pest Management Science*, **56**, 861–866.

Liu, Z. & **Zabkiewicz, J.** (1997) Cuticular uptake of glyphosate into wheat with organosilicone surfactant. *New Zealand Plant Protection*, **50**, 129–133.

Magor, E., **Wilson, M.D.**, **Wong, H.**, **Cresswell, T.**, **Sanchez-Palacios, J.T.**, **Bell, R.W.** ***et al.*** (2023) Selected adjuvants increase the efficacy of foliar biofortification of iodine in bread wheat (*Triticum aestivum* L.) grain. *Frontiers in Plant Science*, **14**, 1246945.

Miller, L.M. & **Dumas, P.** (2006) Chemical imaging of biological tissue with synchrotron infrared light. *Biochimica et Biophysica Acta*, **1758**, 846–857.

Morais, C.L.M., **Lima, K.M.G.**, **Singh, M.** & **Martin, F.L.** (2020) Tutorial: multivariate classification for vibrational spectroscopy in biological samples. *Nature Protocols*, **15**, 2143–2162.

Nadiminti, P.P., **Rookes, J.E.**, **Boyd, B.J.** & **Cahill, D.M.** (2015) Confocal laser scanning microscopy elucidation of the micromorphology of the leaf cuticle and analysis of its chemical composition. *Protoplasma*, **252**, 1475–1486.

O'Keefe, K. (2009) 2. Vegetative growth. In: Edwards, J. (Ed.) *Maize growth & development*. NSW, Australia: NSW Department of Primary Industries, pp. 19–30.

Otzen, D. (2011) Protein-surfactant interactions: a tale of many states. *Biochimica et Biophysica Acta*, **1814**, 562–591.

Rasch, A., **Hunsche, M.**, **Mail, M.**, **Burkhardt, J.**, **Noga, G.** & **Pariyar, S.** (2018) Agricultural adjuvants may impair leaf transpiration and photosynthetic activity. *Plant Physiology and Biochemistry*, **132**, 229–237.

Sandt, C., **Partouche, D.** & **Arluison, V.** (2022) Direct, rapid, and simple evaluation of the expression and conformation of Beta-amyloid in bacterial cells by FTIR spectroscopy. *Methods in Molecular Biology*, **2538**, 235–260.

Sayad, A., **Oduntan, Y.**, **Bokros, N.**, **DeBolt, S.**, **Benzecry, A.**, **Robertson, D.J.** ***et al.*** (2023) The semi-automated development of plant cell wall finite element models. *Plant Methods*, **19**, 3.

Seo, D.J., **Fujita, H.** & **Sakoda, A.** (2011) Structural changes of lignocelluloses by a nonionic surfactant, tween 20, and their effects on cellulase adsorption and saccharification. *Bioresource Technology*, **102**, 9605–9612.

Sharma, S. & **Uttam, K.N.** (2016) Investigation of the manganese stress on wheat plant by attenuated total reflectance Fourier transform infrared spectroscopy. *Spectroscopy Letters*, **49**, 520–528.

Siriwong, S., **Tanthanuch, W.**, **Srisamut, D.**, **Chantarakhon, C.**, **Kamkajon, K.** & **Thumanu, K.** (2022) Performance evaluation of focal plane Array (FPA)-FTIR and synchrotron radiation (SR)-FTIR microspectroscopy to classify Rice components. *Microscopy and Microanalysis*, **5**, 1–10.

Solhi, L., **Guccini, V.**, **Heise, K.**, **Solala, I.**, **Niinivaara, E.**, **Xu, W.** ***et al.*** (2023) Understanding Nanocellulose-water interactions: turning a detriment into an asset. *Chemical Reviews*, **123**, 1925–2015.

Srinivasan, R., **Hoy, M.A.**, **Singh, R.** & **Rogers, M.E.** (2008) Laboratory and field evaluations of Silwet L-77 and kinetic alone and in combination with Imidacloprid and Abamectin for the Management of the Asian Citrus Psyllid, *Diaphorina Citri* (Hemiptera: Psyllidae). *Florida Entomologist*, **91**, 87–100.

Stevens, P.J.G. (1993) Organosilicone surfactants as adjuvants for agrochemicals. *Pesticide Science*, **38**, 103–122.

Tang, X., **Dong, J.** & **Li, X.** (2008) A comparison of spreading behaviors of Silwet L-77 on dry and wet lotus leaves. *Journal of Colloid and Interface Science*, **325**, 223–227.

Tanino, K.K., **Kobayashi, S.**, **Hyett, C.**, **Hamilton, K.**, **Liu, J.**, **Li, B.** ***et al.*** (2013) Allium fistulosum as a novel system to investigate mechanisms of freezing resistance. *Physiologia Plantarum*, **147**, 101–111.

Thumanu, K., **Wongchalee, D.**, **Sompong, M.**, **Phansak, P.**, **Thanh, T.N.**, **Vechklang, K.** ***et al.*** (2017) Synchrotron-based FTIR microspectroscopy of chili resistance induced by *Bacillus subtilis* strain D604 against anthracnose disease. *Journal of Plant Interactions*, **12**, 255–263.

Toplak, M., **Birarda, G.**, **Read, S.**, **Sandt, C.**, **Rosendahl, S.M.**, **Vaccari, L.** ***et al.*** (2017) Infrared orange: Connecting hyperspectral data with machine learning. *Synchrotron Radiation News*, **30**, 40–45.

Toplak, M., **Read, S.T.**, **Sandt, C.** & **Borondics, F.** (2021) Quasar: easy machine learning for biospectroscopy. *Cells*, **10**, 2300.

Toscano, S., **La Fornara, G.** & **Romano, D.** (2022) Salt spray and surfactants induced morphological, physiological, and biochemical responses in *Callistemon citrinus* (Curtis) plants. *Horticulturae*, **8**, 261.

Tran, T.L.C., **Callahan, D.L.**, **Islam, M.T.**, **Wang, Y.**, **Arioli, T.** & **Cahill, D.** (2023) Comparative metabolomic profiling of *Arabidopsis thaliana* roots and leaves reveals complex response mechanisms induced by a seaweed extract. *Frontiers in Plant Science*, **14**, 1114172.

Vongsvivut, J., **Perez-Guaita, D.**, **Wood, B.R.**, **Heraud, P.**, **Khambatta, K.**, **Hartnell, D.** ***et al.*** (2019) Synchrotron macro ATR-FTIR microspectroscopy for high-resolution chemical mapping of single cells. *Analyst*, **144**, 3226–3238.

Wagner, R., **Wu, Y.**, **Czichocki, G.**, **Berlepsch, H.v.**, **Weiland, B.**, **Rexin, F.** ***et al.*** (1999) Silicon-modified surfactants and wetting: I. Synthesis of the single components of Silwet L77 and their spreading performance on a low-energy solid surface. *Applied Organometallic Chemistry*, **13**, 611–620.

Willick, I.R., **Stobbs, J.**, **Karunakaran, C.** & **Tanino, K.K.** (2020) Phenotyping plant cellular and tissue level responses to cold with Synchrotron-based Fourier-Transform Infrared Spectroscopy and X-ray Computed Tomography. In: Hincha, D. & Zuther, E. (Eds.) *Plant Cold Acclimation: Methods and Protocols. Methods in Molecular Biology*. NK: Humana New York, pp. 141–159.

Willick, I.R., **Takahashi, D.**, **Fowler, D.B.**, **Uemura, M.** & **Tanino, K.K.** (2018) Tissue-specific changes in apoplastic proteins and cell wall structure during cold acclimation of winter wheat crowns. *Journal of Experimental Botany*, **69**, 1221–1234.

Yang, J. & **Yen, H.E.** (2002) Early salt stress effects on the changes in chemical composition in leaves of ice plant and Arabidopsis. A Fourier transform infrared spectroscopy study. *Plant Physiology*, **130**, 1032–1042.

Zhang, Y., **Zhang, G.** & **Han, F.** (2006) The spreading and superspeading behavior of new glucosamide-based trisiloxane surfactants on hydrophobic foliage. *Colloids and Surfaces A: Physicochemical and Engineering Aspects*, **276**, 100–106.

Zhao, Q., **Yang, Z.**, **Zhou, Z.**, **Yang, Y.** & **Wang, W.** (2024) Toxicity mechanism of organosilicon adjuvant in combination with S-metolachlor on *Vigna angularis*. *Journal of Hazardous Materials*, **480**, 135978.

Zheng, L., **Cao, C.**, **Chen, Z.**, **Cao, L.**, **Huang, Q.** & **Song, B.** (2021) Efficient pesticide formulation and regulation mechanism for improving the deposition of droplets on the leaves of rice (*Oryza sativa* L.). *Pest Management Science*, **77**, 3198–3207.

Zhou, Z., **Cao, C.**, **Cao, L.**, **Zheng, L.**, **Xu, J.**, **Li, F.** ***et al.*** (2018) Effect of surfactant concentration on the evaporation of droplets on cotton (*Gossypium hirsutum* L.) leaves. *Colloids and Surfaces B: Biointerfaces*, **167**, 206–212.